Report on the results obtained during the second year at midterm of the ESSnuSB Feasibility Study for Employing the Uniquely Powerful ESS Linear Accelerator to generate an Intense Neutrino Beam for Leptonic CP Violation Discovery and Measurements

Period covered by the report: **from 01/01/2019 to 31/12/2019**

Date: **28/02/2020**

1. Introduction

The key objective of the ESSνSB (European Spallation Source Neutrino Super Beam) Design Study is to demonstrate the feasibility of using the European Spallation Source (ESS) proton linac to produce the world's most intense neutrino beam concurrently with the 5 MW proton beam to be used for the production of spallation neutrons. In order to achieve this, ESSνSB's high-level objectives are:

1) to specify and design the necessary upgrades to the current ESS linear accelerator in order to raise the average beam power from 5 MW to 10 MW by inserting, between the proton pulses for spallation neutron production, additional H- ion pulses for neutrino production,

2) to design an intermediate proton-beam storage ring so as to match the beam parameters to the requirements of the hadron collector, which is needed for the generation of well-focused neutrino beam,

3) to update and adapt the existing design of the pion production target and collection, the pion to neutrino and muon decay tunnel and the Water Cherenkov far detector, already studied in detail in the FP6/FP7 projects CARE, EUROν, LAGUNA and LAGUNA-LBNO, to the specific requirements of ESSνSB,

4) to study the design of a near detector to be used for both the monitoring of the neutrino beam flux and for the measurements of the neutrino cross-sections of interest, with the aim of minimising the systematic errors of the neutrino oscillation measurements, as well as to optimise the far Water Cherenkov detector design,

5) to carry out an investigation of the geological characteristics and logistical challenges of the currently preferred site for the underground far detector, which is located at a distance from ESS corresponding to the second neutrino oscillation maximum, and also to consider possible alternative sites.

1. The Linac upgrade

Introduction

The ESSnuSB Linac upgrade consists of the modifications of the ESS proton linac needed in order to be able to produce and accelerate interleaved pulses of H⁻ beam for the generation of the proposed neutrino super beam while the acceleration of protons for the production of spallation neutrons remains un-interrupted.

The linac upgrade study

The baseline linac energy, current and pulse structure has been defined with more details in collaboration with other partners in the project, and is being refined through discussions with all the concerned stakeholders. The Low Energy Beam Transport (LEBT) and Medium Energy Beam Transport (MEBT) lines have been modelled and simulated, the work is progressing well. A detailed study of the modifications needed on the modulators was performed, showing the upgrade possibility paths for the modulators, with an evaluation of the energy efficiency of each option, their cost and their added footprint on the klystron gallery. The study of the H⁻ beam stripping continued with simulations of the beam transport and evaluation of the loss magnitude for the baseline beam parameters.

Modifications to the operation of the proton driver

A pulsing scheme with an overall 28 Hz macro-pulse structure is selected as the baseline design, option A in the Figure 1 below. Other pulsing schemes have also been considered, options B and C, where the H⁻ beam is pulsed at 70 Hz. This however results in a higher total load of the RF system, since the filling time of the superconducting cavities is in the order of 0.3 ms. Option B, with a pulse length of up to 1.3 ms, has the advantage that it allows for an even lower beam current of about 30 mA, relaxing the demands on the ion source requirements and reducing intra beam stripping losses.
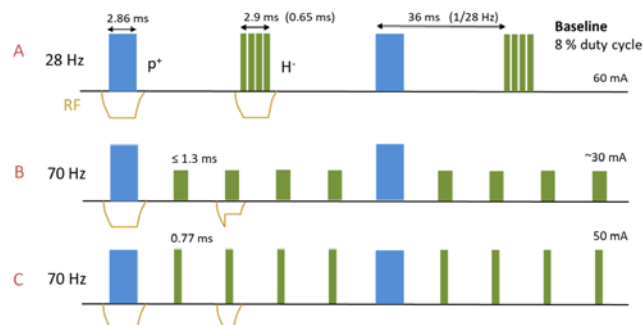

Figure 1: Pulsing options, with option A chosen as the baseline design.

A baseline pulse structure of the linac, which defined the pulse structure and current in the ring and the repetition rate of the target has been set. The work is still ongoing in finding the optimum solution. The results have been presented and published in proceedings to the International Particle Accelerator Conference IPAC 2019.

H⁻ source choice and installation study

We have studied the Penning source at RAL and the RF source at SNS in detail since these have been identified as being the most promising ion sources to meet the requirements of the future ESSνSB ion source. For the baseline option A, with long pulses of 3 ms, the closest to match is the Penning source at RAL. However, this source type is quite service demanding and requires relatively high amount of Cs. The RF source at SNS has a higher lifetime and use less Cs. For both ion sources, it remains to be shown that they can deliver long pulses. Pulse flat-top is sufficient to maintain a stable flat-top current of 80 mA in 3 ms at 14 Hz, within a few percent.

For the alternative option B and C, 50-80 mA, ~1 ms at 70 Hz, both sources are feasible alternatives. The RF source seems the most interesting alternative from the lifetime point of view, and the requirements are almost met by the state-of-the-art ion sources at SNS and J-PARC.

We have recently started collaborations with both RAL and SNS, in order to follow the development and find out if there are any areas of R&D that need to be covered in order to reach the requirements of the ion source for ESSνSB. As of today, neither of these sources meet the requirements of the ESSνSB ion source. However, steady improvements in performance of the ion sources lead to the expectation that they will meet the requirements within the schedule of the ESSνSB project.

Progress has been made on the choice of the H⁻ source and engagement of the scientific community even beyond the partners of the ESSνSB project.

Acceleration of the H⁻ beam

Simulations of the beam transport through the LEBT and RFQ have been carried out utilising the TraceWin software. Two possible layouts have been analysed: either with the H⁻ ion source at an angle of 60 degrees to the existing proton ion source, or with the proton and H⁻ ion sources at ± 30 degrees with respect to the rest of the linac. The simulations show that the design with a beam transport of ±30 degrees is much less sensitive to the initial ion source distribution and the degree of space charge compensation, than the 60-degree design.

The beam distributions obtained from TraceWin for the upgraded ESS linac (from the nominal 2.0 GeV to 2.5 GeV) were further post-processed to analyse the loss rates from stripping. Although the loss rates from stripping are fractional and are not expected to affect the beam dynamics, the activation due to stripping of H⁻ and the resulting loss of H⁰ can be considerable, especially at high energies.

The beam distributions from TraceWin have been used for evaluating the H⁻ losses and the findings were presented as an oral presentation at the International Workshop on Neutrinos from Accelerators NUFACT2019. The contribution to the proceedings of this workshop is in preparation, its publication is expected in 2020.

Stripping of H⁻ ions

The stripping mechanisms of intra-beam collision have been identified and evaluated. The mechanisms include: Lorentz stripping by the magnetic field, intra beam scattering from the other particles in the beam, interaction with blackbody radiation, and rest gas scattering.

Ongoing studies concern optimizing the beamline parameters of the interleaved proton and H⁻ species, retooling existing equipment for the task, and analysing the cost impact of different sub-pulsing schemes in terms of cooling and facility power requirements.

The prevalent stripping mechanism of intra-beam collision is expected to induce losses within the prescribed limit of 0.5 W/m for the ESS linac with nominal design parameters. In general, since prohibitive losses are not expected due to H⁻ stripping or mode-resonance effects, beam dynamics concerns in the linac are not likely to hinder the feasibility of ESSvSB.

The results have been presented as an oral presentation at the International Workshop on Neutrinos from Accelerators NUFACT2019. The contribution to the proceedings of this workshop is in preparation, its publication is expected in 2020.

Beam chopping

The possible side effects of the proposed chopping scheme, in the form of excitation of the Higher Order Modes (HOM) in superconducting cavities by creating extraction gaps for the accumulator ring in the linac, have been studied by doing simulations of the beam degradation. The conclusion is that the suggested chopping scheme does not create additional degradation of the beam.

The chopping scheme required for the ESSvSB does not excite dangerous HOMs and is not a show stopper in beam preparation for injection to the ring. The results have been presented and published in proceedings to the International Particle Accelerator Conference IPAC 2019.

Power doubling

An assessment has been made for potential solutions of the high-power modulators of the ESSvSB project regarding the different pulsing options: comparing upgrade of the present SML modulators to handle the increased average power, and alternatively adding separate modulators based on conventional pulse transformer technology.

Both alternatives have been found technically feasible. Upgrading the SML modulators would require significantly less additional space (footprint) and is approximately two times less expensive than the option based on procuring an additional set of pulse transformer-based modulators in terms of investment cost.

2. The Accumulator

Introduction

The work on the Accumulator consists of the design of a transfer line, an accumulator ring and a switchyard in order to transport and transform the long pulses of H- ions from the linac to short pulses of protons to the target, with minimum losses.

During the second year of the project, it has been concluded that the most likely accumulator operation scheme is to have a single accumulator ring collecting each linac pulse in four separate batches separated at roughly 1 kH. This configuration meets best the boundary conditions of the linac and is acceptable to the target station.

The accumulator ring lattice design has been consolidated. Second order improvements are being added. An optimization study of the multi-turn injection process has been completed. A round, close to uniform

beam with geometric emittance of 70 mm mrad, can be produced using correlated phase space painting. This smaller emittance, as compared to previous results, will facilitate beam extraction and switching.

Methods of mitigating high temperatures in the stripper foil have been examined. Mismatched injection in combination with longitudinally split foils can reduce the peak temperature significantly.

Two configurations of the beam switchyard design can transport the beam from the accumulator to the targets with negligible losses. The technical feasibility of the switchyard design is under study.

The Lattice design of the ring

The lattice design has been consolidated through beam optics and multi-particle simulations. Only minor changes to the bare lattice have been made during 2019

The ring can accumulate 2.23×10^{14} particles during roughly 500 turns and produce a beam with a final geometric emittance of down to 60 π mm mrad, including almost 100% of the beam particles. This emittance is a factor two lower than what was previously targeted. A lower emittance will facilitate beam extraction and transport through the switchyard to the target. However, a smaller emittance in general also means more stray foil hits from particles in the circulating beam, which in turn contributes to the heating of the stripper foil. To this end, the final emittance may be up to 80 π mm mrad.

The total tune spread expected with this smaller beam is below 0.05, which means that space charge is no longer a worry in the accumulator ring design. The main challenges of the design at present is to control the beam loss and to find an H^- stripping scheme that is reliable over time. The design of a two-stage collimation system to meet the first challenge has started.

The choice of radiofrequency (RF) cavities for longitudinal beam containment has been studied in detail. A barrier RF cavity has been identified to be the best choice since it simultaneously provides effective preservation of the 100 ns particle-free gap required for extraction and ensures that the energy spread in the beam is kept low. A dual-harmonic cavity with low RF voltage has been identified as an acceptable alternative solution.

The natural chromaticity of -11/-12 can be fully corrected using five sextupole magnets of moderate strength in each arc. The effect of the chromaticity correction on the dynamic aperture is under investigation.

The Linac-to-accumulator transfer line, injection scheme and ring location

The overall layout of the complex needed for ESSvSB has been studied and a number of alternatives exist. In the most attractive alternative, shown in Figure 2, the linac-to-accumulator transfer line consists of a relatively short arc section followed by a straight section. Limiting the length of the arc is important to reduce the particle loss caused by Lorentz stripping. In this alternative, the extraction from the ring is placed on the opposite side of the ring from the injection. It provides ample space for the extraction and beam switchyard.

The ESS linac is placed 5 m below ground level but an additional 5 m layer of soil has been added on top to provide sufficient shielding. The accumulator ring will be placed so that there is 10 m of soil on top of the ring. Most likely the ring will be put 10 m below ground so that the ring is "invisible" on the ground level. This would imply that the transfer line would have to include a vertical shift of the beam, either through a continuous slope or through a dog leg.
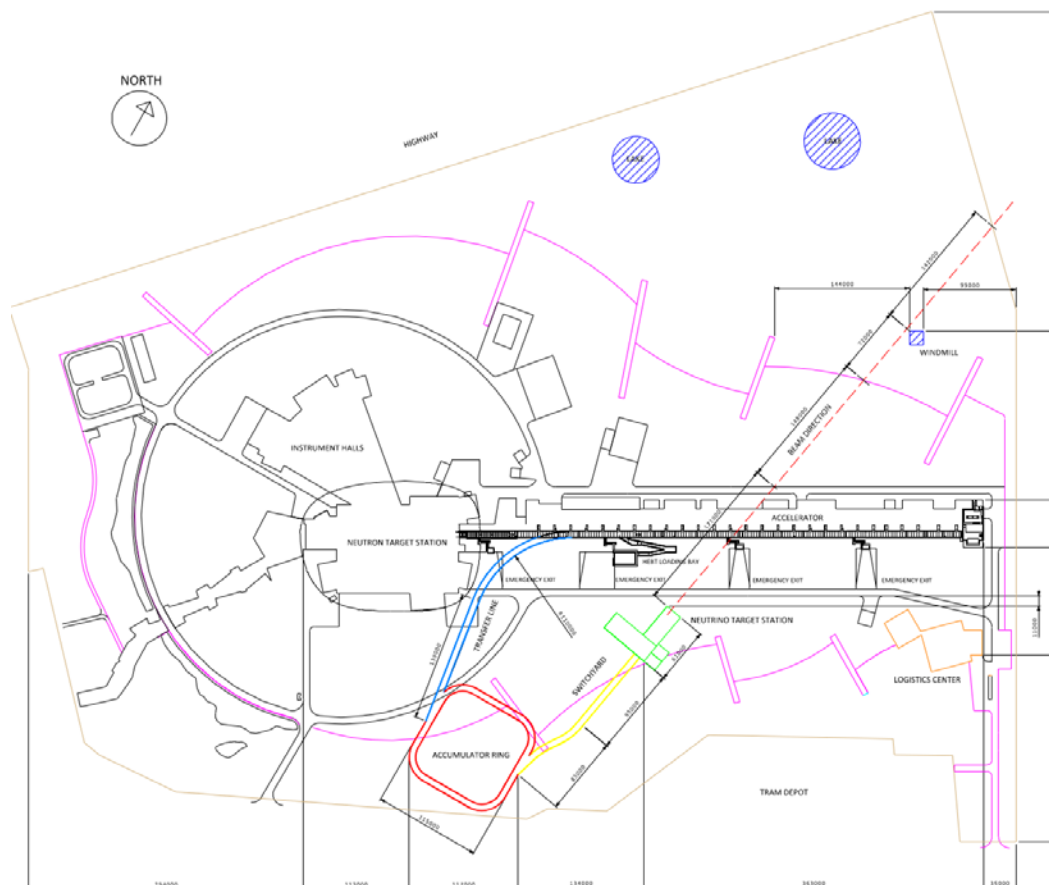
Figure 2: The suggested layout of the ESSvSB transfer line, accumulator ring, switchyard and target station on the ESS site.

The Study of H⁻ ion stripping

Substantial effort has been put into studying the injection and the H⁻ stripping, in particular of the foil-stripping technique. The long-term performance of the stripper foil is considered as a major challenge in high power accumulator rings like this. The peak temperature in the foil must be kept low since sublimation from the foil rises quickly with increasing temperature. Several ways of keeping the peak temperature low during injection have been studied. Firstly, the injection painting process, where the injected beam gradually fills the beam phase space in the ring, has been studied and optimized. The painting is designed by varying the strength of the injection kicker magnets during each fill. This is done with two main objectives: a) to produce a beam distribution that creates good conditions for beam stability in the ring and, at the same time, meets the requirements of the target; b) to keep stray foil hits from circulating, i.e. already stripped, particles to a minimum. The former means a smooth distribution, close to uniform. Since the target has a circular cross section, a round beam, which can be obtained by anti-correlated painting, is preferred over a square beam, which can be obtained by correlated painting. The average number of foil hits per particle is on the other hand higher in this case (7.5) compared to the case for correlated painting (5.2). By allowing for a larger final emittance the number of foil hits can be somewhat reduced. The final emittance will be chosen to comply with the requirements of several subsystems, such as the stripper foil, the machine acceptance and magnet apertures, beam stability and loss, extraction and switchyard.

Figure 3 shows how the orbit bump amplitude varies during one fill for the optimized painting scheme. With this orbit bump, the density distribution, displayed in Figure 3, is close to uniform which reduces

space charge forces in the beam. In addition, a uniform beam on the target is desirable from a thermal point of view. The top row in Figure 4 shows the density distribution resulting from correlated painting where the circulating beam in both planes is moved away from the injection point as the injection proceeds. The bottom row shows the result of anti-correlated painting, where the beam is moved away from the injection point in the horizontal plane and towards the injection point in the vertical direction. Anti-correlated painting produces a round beam, which is also better for the thermal response of the target.
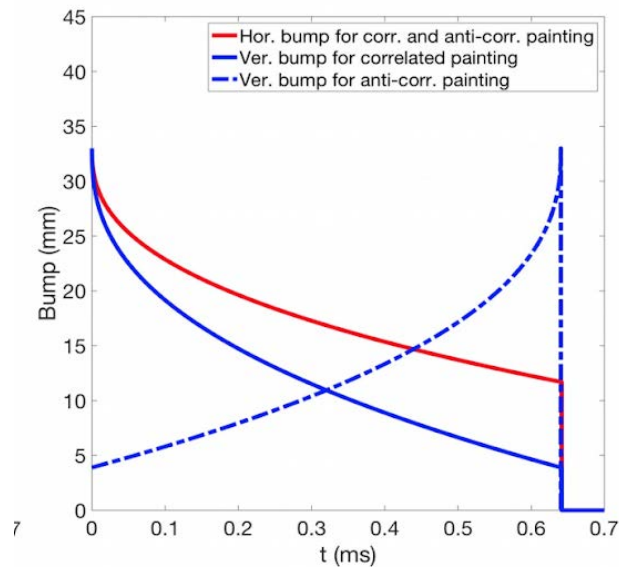

Figure 3: The horizontal and vertical orbit bump amplitudes as they vary during one fill. The dashed line represents anti-correlated painting where the beam is progressively moved closer to the injection point in one plane and away from the injection point in the other plane.
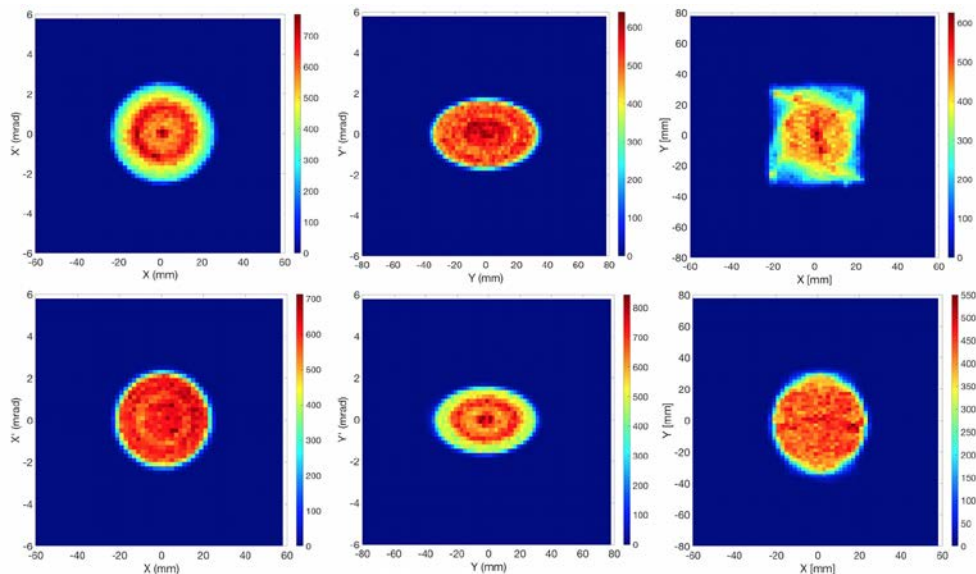

Figure 4: The density distribution, from left to right, in horizontal phase space, vertical phase space, and real space, obtained using the orbit bump depicted in Figure 2. The top row shows the result for correlated painting, resulting in a square beam in real space. The bottom row shows the preferred distribution, obtained with anti-correlated painting.

By optimizing the injection, the hottest spot on the stripper foil is shifted from the edge, where the stray hits occur, to the centre, where the actual stripping takes place. The peak temperature can be further reduced by making the injected beam spot larger, either by increasing the optical beta function in the ring at the injection point, β_m, or through a mismatched injection, i.e. by making the beta function of the incoming beam, β_i, larger than β_m. Figure 5 shows an example of the injected beam distribution in real space and the corresponding stripper foil dimensions for two cases: a matched injection ($\beta_i=\beta_m$) and mismatched injection ($\beta_i=2\beta_m$). Figure 6 shows the resulting energy deposition in the foil for both matched and mismatched beam injection. We conclude that using a mismatched injection can significantly reduce the energy deposition at the centre, which leads to a reduction of the peak temperature of more than 400 K.
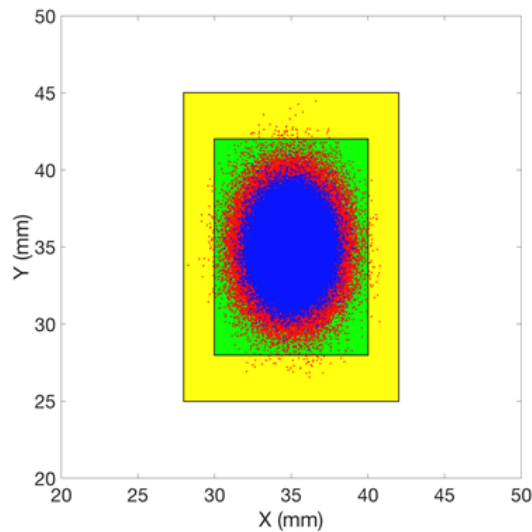

Figure 5: An example of the injected beam distributions in real space and the corresponding stripper foil dimensions. Blue spot and green area are for matched injection; red spot and yellow area are for mismatched injection with $\beta_i/\beta_m=2$.
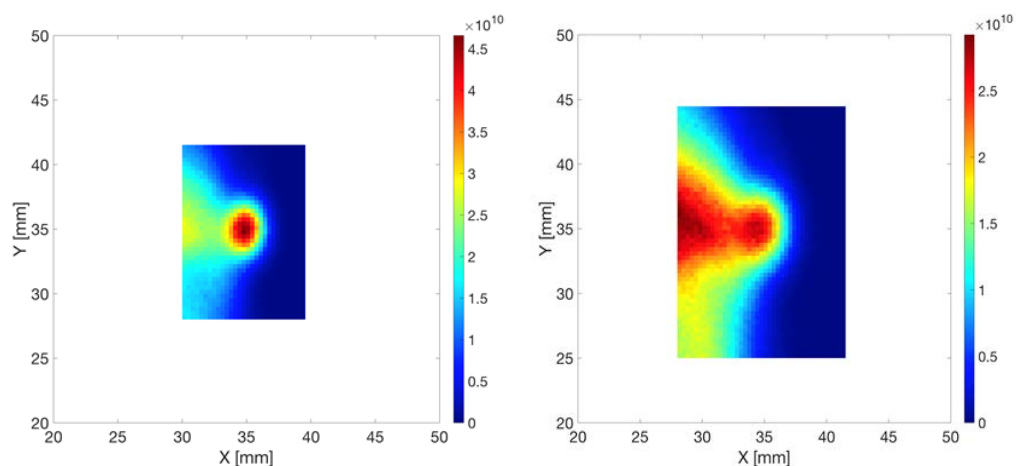

Figure 6: Energy deposition (J/m^3) in the foil for four beam batches using matched beam injection (left) and mismatched beam injection with $\beta_i/\beta_m=2$ (right).

Another way of reducing the heating of the stripper foil is to replace the single foil with several thinner foils that are traversed by the beam in sequence. Figure 7 shows the results of a calculation of the foil

temperature for one thick foil and four thinner foils both at centre and inner edge for matched and mismatched injection. Simulations have shown that by replacing a foil with thickness 500 µg/cm² (corresponding to a stripping efficiency of 99%) with 4 foils of thickness 125 µg/cm² each, the peak temperature in the foil can be reduced by over 600 K. If both of the methods are adopted, meaning mismatched injection and split foils, the peak temperature can be reduced by around 900 K and the final peak temperature can be below 2000 K. Further studies of this scheme are ongoing.
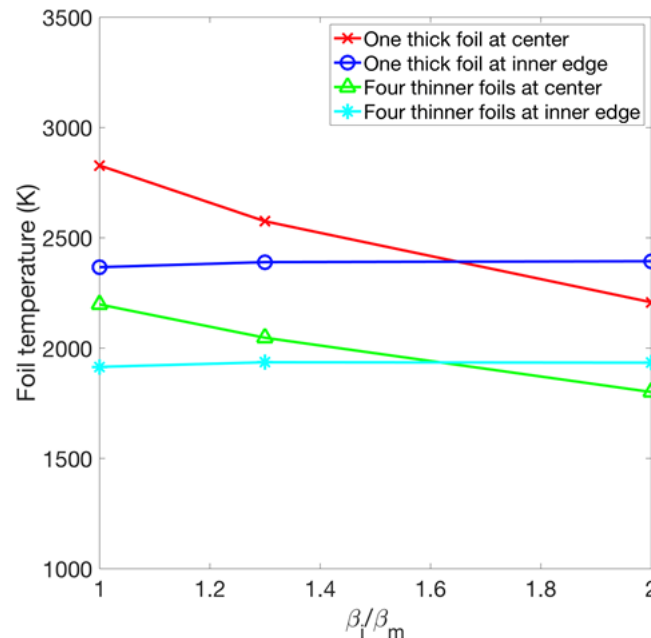

Figure 7: Results of foil temperature calculations for one thick foil and four thinner foils, both at the centre and at the inner edge of the foil, for matched (β_i/β_m=1) and mismatched beam injection with β_i/β_m =1.3 and β_i/β_m=2.

The peak temperature in the stripper foil can also be reduced by shifting the point of injection during a fill. This scheme, of which the technical feasibility is still to be investigated, has been tested through simulations with promising results. By gradually moving the injection point along a diagonal stretch of about 20 mm, and by following with the circulating beam, the peak steady-state temperature can be kept below 1800 K, which is considered operationally safe. These studies will continue during the coming year.

The long-term plan is to use laser-assisted stripping in the ESSνSB accumulator. However, the resources allocated to the WP3 do not make room for any experimental work on this topic. Instead, contact has been established with the SNS where tests are ongoing. Members from the WP3 team have been invited to observe upcoming tests of a new setup with laser-assisted stripping. These tests will help identifying where further efforts are needed in order for laser-stripping to meet the high requirements of the ESSνSB.

The Extraction Scheme

The extraction scheme is under study at the moment. During the first stage of the extraction design, important requirements have been identified. A preliminary version of the extraction optics has been made. This design will now be optimized.

The SNS accumulator uses vertical extraction followed by a horizontal septum. We will consider this solution as well as other possibilities.

The pulsing of the extraction kickers is demanding in the baseline accumulator operation scheme, where there is less than 0.9 ms between the extraction of one batch and the extraction of the following batch. Whether several pulse forming networks rather than just one will be needed to power the extraction magnets, is under investigation.

The Design of the beam switchyard

The space available for the beam switching was unknown. During 2019, the ambition of the switchyard design was to reduce the necessary length of the switchyard as much as possible. Two designs exist, with different switching schemes. Configuration 1 has been reduced in length from 43 to 18 m while configuration 2 measures 26 m, compared to the previous 72 m. Using the beam distribution at the exit of the accumulator as input in the beam switchyard, the beam can be transported through the switchyard with negligible beam loss while meeting the beam size requirement on the target.

The reduced length of the switchyard results in a stronger magnetic field in the switching dipoles. At the same time, the switching must be fast since there is less than 0.9 ms between each beam batch. The feasibility of these magnets and their power supplies are being investigated. Alternative techniques, such as using fast kickers in combination with a septum, are also considered. In addition, the overall layout considered at present (Figure 2) permits a longer switchyard. The switchyard design is now being revisited in order to determine the total length required for the switching if conventional technology was to be used.

The last active elements in the switchyard must be protected against particle showers from the downstream target station. To this end, the four collimator blocks that have the task of performing the final cleaning of beam halo particles before the target, have been replaced by a large block with four slits, one for each line going to a separate target station. In this way, the collimator block protects the machinery in a dual manner: the target station is protected against beam halo from the switchyard and the switchyard magnets are protected against backscattered particle showers from the target.

FLUKA simulations have been performed in order to estimate the particle flux from the target, and the resulting energy deposition in the last magnets of the switchyard. This work is ongoing.

n case of failure of one or several dipole switching magnets, a beam dump will be required. The dimensions of such a beam dump are being investigated.

3. The Target Station

Introduction

The Target Station Facility is the key element of the ESSvSB project which will convert the 5 MW proton beam to an intense neutrino beam. The technology is based on four solid targets, each embedded in a magnetic horn which are the usual technology used in Super Beam experiments. The target station, called "four-horn system", is submitted to severe working conditions in terms of energy deposition and vibrations imposed by the pulsed proton beam and represents a real challenge in terms of physics and engineering design. In addition, the facility hosting the target station will be submitted to an intense secondary particle flux producing a high energy deposition and material activation in the whole facility. As a consequence, the design has to be conceived with secondary elements such as a power supply delivering the high intensity current to the horns, an efficient system to cool the whole building, hot cells

and morgue to repair and store radioactive elements. The objectives defined in the WP4 framework are defined to reach an efficient design of the target station facility.

Adapt the EUROv design target station to the ESSvSB requirements

For several reasons, the geometry of the target station has been modified compared to the EUROv one by relocating the Power Supply Room outside of the facility (See Figure 8):

- Issue: even if the Four-Horn System is removable by opening the top of the iron shielding in a specific chamber confining the radioactivity, the proximity of the power supply above the decay tunnel could nonetheless raise the question of safety. Locating the Power Supply room outside the main building appears a good solution for the Power Supply lifetime, to limit the workers' exposition and also to prevent additional costs due to the safety requirements imposed by the Swedish regulations.
- Better accessibility for maintenance work.
- The Horn Power supply room will be located above the Beam Switchyard room (instead of above the decay tunnel) to favour the synchronisation with the future Beam Switchyard power supply, not designed at the present time.
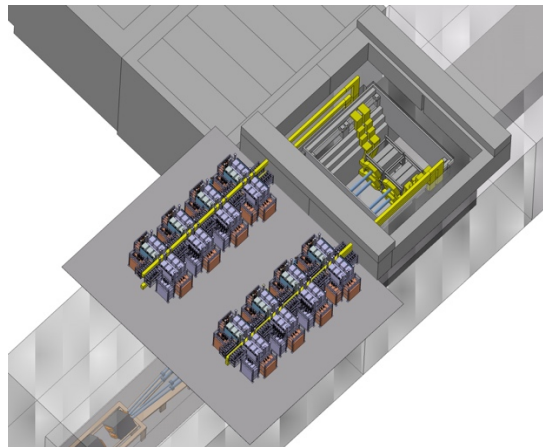

Figure 8: Location of the Horn Power Supply room.

Caveat: the location of the power supply room is limited by the strip line length.

Target integration

Both the analytical and numerical studies concerning the target integration have begun during the concerned period. Numerous analyses have been performed regarding the following topics: the power deposition and distribution inside the target after the beam impact, granular packing and sphere temperature increase, as well as the feasibility of target cooling using gaseous helium.

Studies concerning the target cooling using helium were performed under the assumption of constant power distribution inside the target and the helium flow both in the axial and transverse direction. These analyses provided information regarding the temperature increase inside the target and the issues arising when considering the direction of the flow. Specifically, the flow in the axial direction for cooling purposes has posed problems due to an enormous value of calculated pressure drop between the inlet and the outlet.

The analytical study of the target focused on deriving a simplified model of heat transfer and target cooling. This model in turn could be used at the next analysis stages in order to quickly estimate the temperature levels in the target and ascertain the correctness of the analysis. Both in the numerical and the analytical studies, it was assumed that the behaviour of gas inside the granular target can be modelled via the porous medium definition (introduction of additional viscous and inertial resistance terms in the momentum equations) and that the gas itself is ideal and compressible. The results obtained from the analytical and numerical studies, for the transverse flow under the constant power distribution assumption were comparable.

In subsequent studies, the power distribution in the target after the beam impact obtained from the calculations performed in FLUKA has been considered. In these numerical analyses, the focus was placed on determining the effectiveness of cooling by helium in the transverse direction and the resulting temperature distribution inside the target. At first, these tests were performed under the assumption that the width of the inlet and the outlet gap is constant along the length of the target. In such a case, it was shown that more helium tends to flow in the region of lower temperature, thus diminishing the effect of cooling on target. Modifications in the shape of both the inlet and the outlet were introduced in the numerical model in order to enforce higher mass flow in the sections that absorbed more power and as such reached higher temperature levels. An example of the steady-state temperature results under such conditions (approximate power distribution, transverse flow 100 g/s, modified inlet and outlet width (differing by section) is shown in Figure 9.
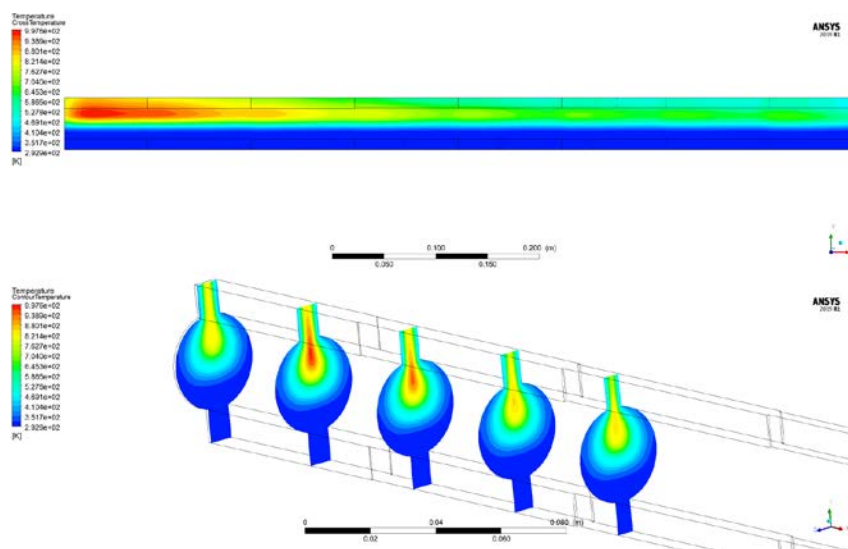

-

Figure 9: Helium temperature distribution in target during cooling in transverse direction through slots of differing width.

The focus of current numerical analyses is to determine the heat and temperature distribution for different slot sizes and shapes, more complex models (3-dimensional target models with inlet and outlet holes), mixed granular-monolithic target and segmented targets.

The analytical model of target cooling has been developed. The verification of the model was performed using Finite Element Analysis. These calculations provided the results concerning the cooling of the

target. This task is covered by milestone MS17 and deliverable D4.4, which come towards the end of the project. The target studies and its integration within the horn will continue during the coming months.

Optimization of the horn type hadron collector

The initial design was fixed in the EUROν project with working conditions close to the present ones. The optimization procedures are driven by the physics performances but also by the mechanical constraints. Even if the best design consists in using a magnetic horn with surrounding collector, it was proved that the working conditions of such double horn device cannot technically be achieved and a single horn has been considered. According to this study, although the physics optimization procedure results indicate no need for a major horn change in the shape compared to the EUROν horn, some improvements of physics performance have been observed.

Physics optimization

The methodology used for the optimization is based on the variation of EUROν horn initial geometry shape with respect to the following parameters:
1. Rescaling of the horn shape (Scale Factor),
2. Total length of the horn (L_{TOT}),
3. Total radius of the horn (R_{TOT}).

The parameter evolution is illustrated in Figure 10, which shows the profile of the horn shape after rescaling, after changing the total length and the radius.
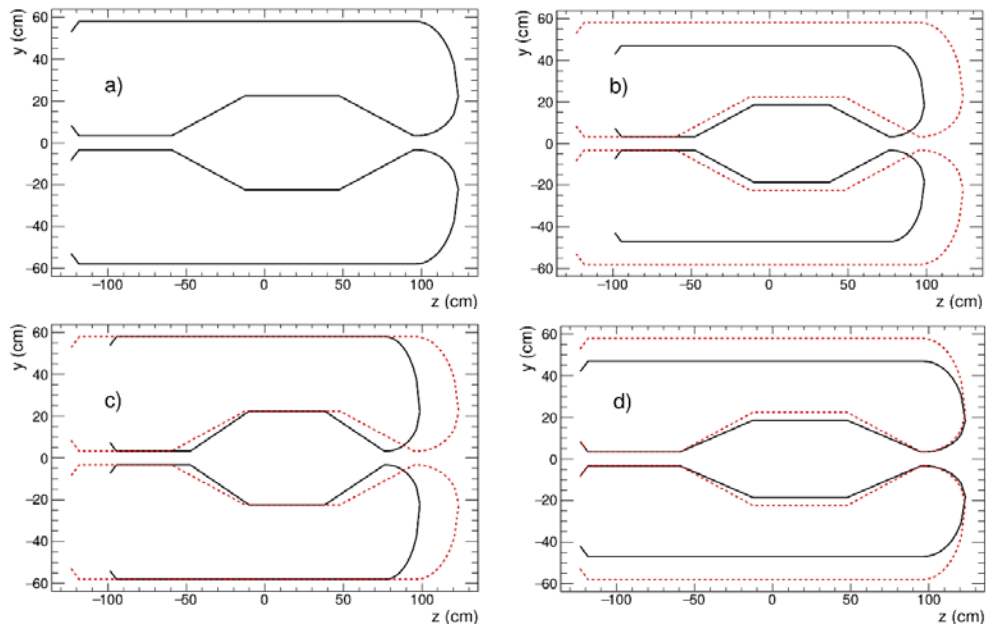

Figure 10: Horn shape profile after rescaling, according to the definition of parameters 1)-3), in particular the baseline (a) and the shape profile after rescaling of the shape (b), the total length (c) and the radius (d) are shown. For panels b)-d), the baseline shape is shown with red dotted lines.

One of the Figures of Merit (FOM) considered in this parametric study is defined by the ratio between real Horn Focusing (HF) and Perfect Focusing (PF), the latter defined as the ideal case, in which all the pions produced in the forward direction are focused in the direction of the detector. Figure 11 shows the muon neutrino flux for the current baseline, in the case of no-focusing, normal focusing and perfect focusing. When studying the dependence on the geometry of the decay tunnel, other Figures of Merit have been the ratio of electron neutrinos over the muon neutrinos and the mean energy of the muon neutrinos.
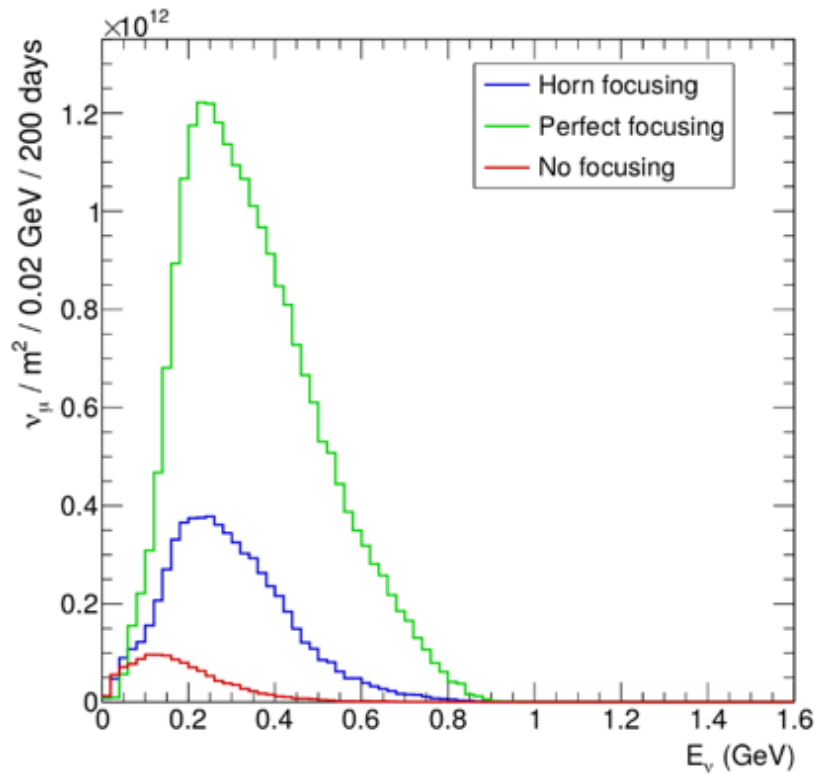

Figure 11: Neutrino fluxes obtained for no focusing, normal focusing and perfect focusing conditions.

The impact of the physics optimization is evaluated by looking at the evolution of the ratio of the Horn Focusing (HF) over the Perfect Focusing (PF). It was observed that the effect of increasing the scale of the horn results in a reduced focusing efficiency, the main contribution to this reduction comes from increasing the length.

The optimisation procedure is based on the reasonable assumption to have focusing efficiency with a more intense pion flux in the decay tunnel. These modifications affect the flux intensity and contamination in terms of flavours. The precision to the CP violation sensitivity has been re-estimated by GLOBES software and it is summarized in Figure 12.
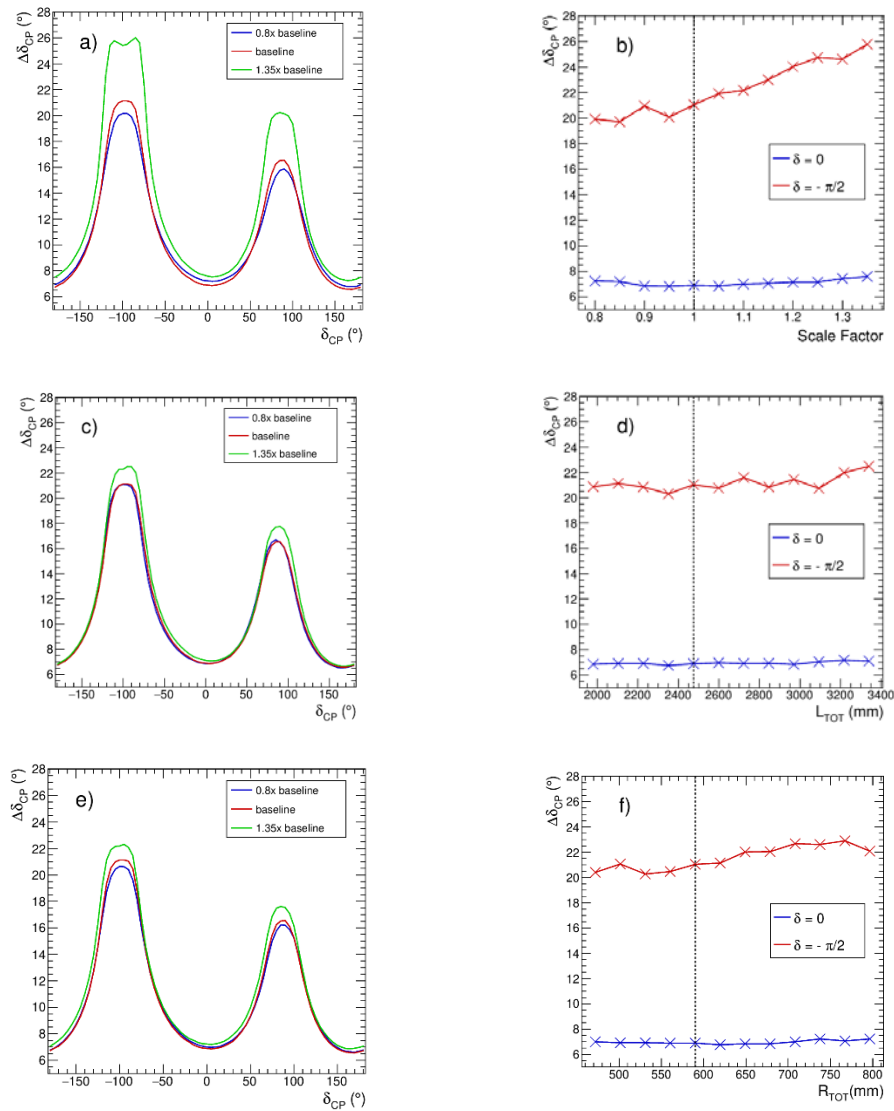
Figure 12: Uncertainty on the measurement of the δ_CP phase (left panel) and uncertainty for the values of δ_CP 0 and –π/2 (right panel) for different values of the scaling factor (a, b), total length (c, d) and radius (e, f) of the horn. The dotted line indicates the baseline parameter values.

The results show a certain stability of the present design with respect to the optimisation procedure. Complementary investigations related to the facility dimensions have been considered in the optimisation process, such as the width of the decay tunnel and the length of the tunnel, changing also the neutrino flux intensity and contamination in other flavours. This contamination does not seem to have a significant impact on the sensitivity of the experiment.

Engineering aspects of the horn shape

Apart from physics performance, technical aspects of the horn design must also be considered, taking into account the severe conditions under which the magnetic horn will be operated. The horn feasibility study must identify and reduce the possible problems that can influence its operation. The design of the horn is an iterative process that takes both the physics and engineering aspects into consideration.

Several horn geometries have been studied from the point of view of the level of dynamic stress, brought about by magnetic forces, Joule heating and secondary particle deposition in the horn skin. The finite element code ANSYS was used in the analysis, thanks to its extensively coupled-field capabilities. A procedure was developed, which enables the importing of the geometry used in physics calculations into ANSYS.

Example results of the magnetic flux density and the von Mises stress are shown in Figure 13. The plots were obtained for a single half-sinusoid current pulse of amplitude 350 kA and 100 μs total duration.
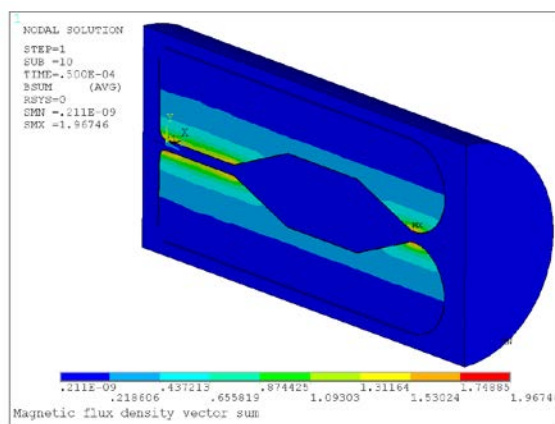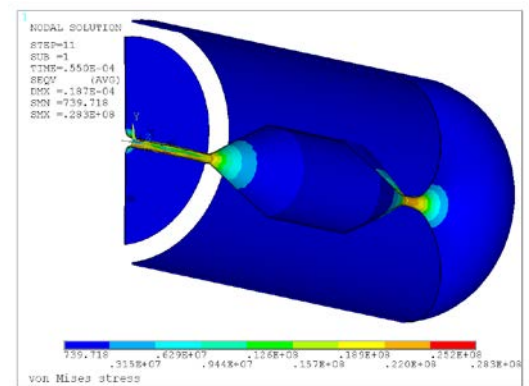

Figure 13a)   **Figure 13b)**

*Figure 13*a): Magnitude of magnetic flux density vector at t = 50 μs (peak current). Figure 13b): Von Mises stress at t = 55 μs.

Table 1 gives a comparison of the maximum von Mises stress and maximum displacement, for three different horn geometries. These geometries are differed mainly in the shape of the end plate; the horn length and diameter were taken from the physics studies. In the table, design 1 had a flat end plate, whereas designs 2 and 3 used a rounded end. Design 3, the technical drawing of which is shown in **Error! Reference source not found.**, has the lowest stress levels, and it is used as the current baseline shape.
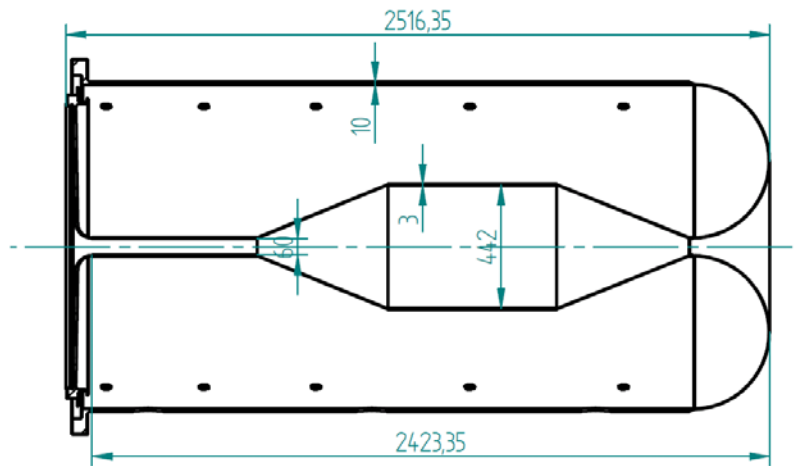
Figure 14: Technical drawing of the baseline horn.

Table 1: Comparison of the maximum von Mises stress and maximum displacement.

Geometry	Max von Mises stress (MPa)	Max displacement (mm)
Design 1	35.5	0.295
Design 2	37.6	0.269
Design 3	28.3	0.123

The stress studies made so far indicate that the dynamic stress due to a single current pulse is at an acceptable level (about 30 MPa). The stress levels can be higher for a sequence of current pulses, especially for near-resonance conditions, should the pulse repetition rate (14 Hz) lie near one of the horn natural frequencies. To avoid this possibility, a spider wire connection between the inner and the outer conductor is being studied.

The chosen horn shape appears to be adequate and feasible for the ESSνSB experiment. The final horn shape will be determined based on both physics and thermomechanical calculations, taking into consideration the target integration inside the horn.

Task 4.5: Horn current pulse generator

According to the WP4 baseline parameters, the horn current pulse generator is foreseen to work at 28 Hz. However, several other pulse schemes, represented in Figure 15(b and c), were proposed by WP2 and WP3, bringing additional difficulties.
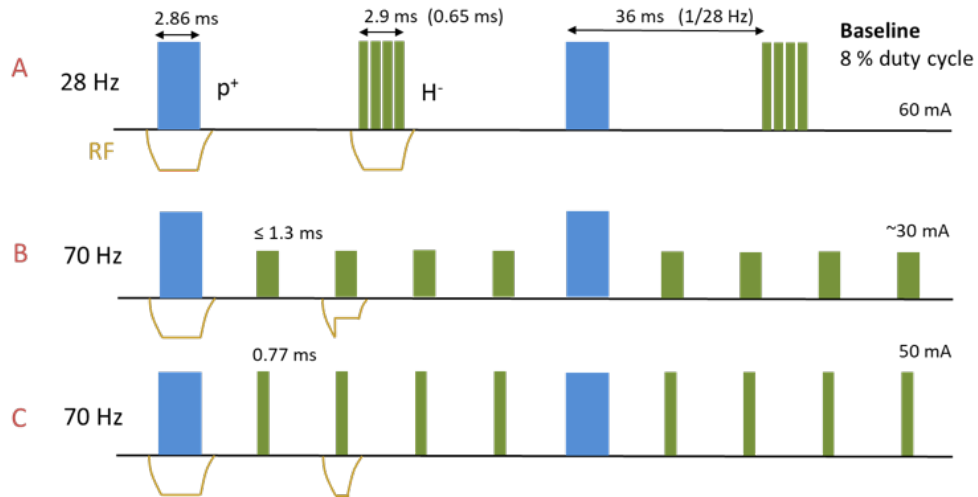
Figure 15: ESSvSB Linac Proton Beam scenarios (scenario A is now the baseline).

These new scenarios require fast switching between the horns, compared to the baseline frequency. The modular approach already used can be employed with some modifications which are summarized below.

For option A

The principle of the PSU (Power Supply Unit) for option A is presented in Figure 16. To provide the 350 kA current for the 4 Horns, 16 modules are necessary. The bench capacitors of 120 µF of the 16 modules are charged during 70 ms to +12 kV (Figure 16). When the charge is high enough, the outputs H1 of Modules 1 to 8 branched in parallel are switched at the same time to provide the 350 kA to Horn1; 750 µs later the same process takes place for the outputs H2 for the Modules 9 to 16 to provide the 350 kA to Horn 2, and so on. The recovery energy made by the 2 mH coil placed in series with a diode start when the voltage of the bench capacitors becomes negative.
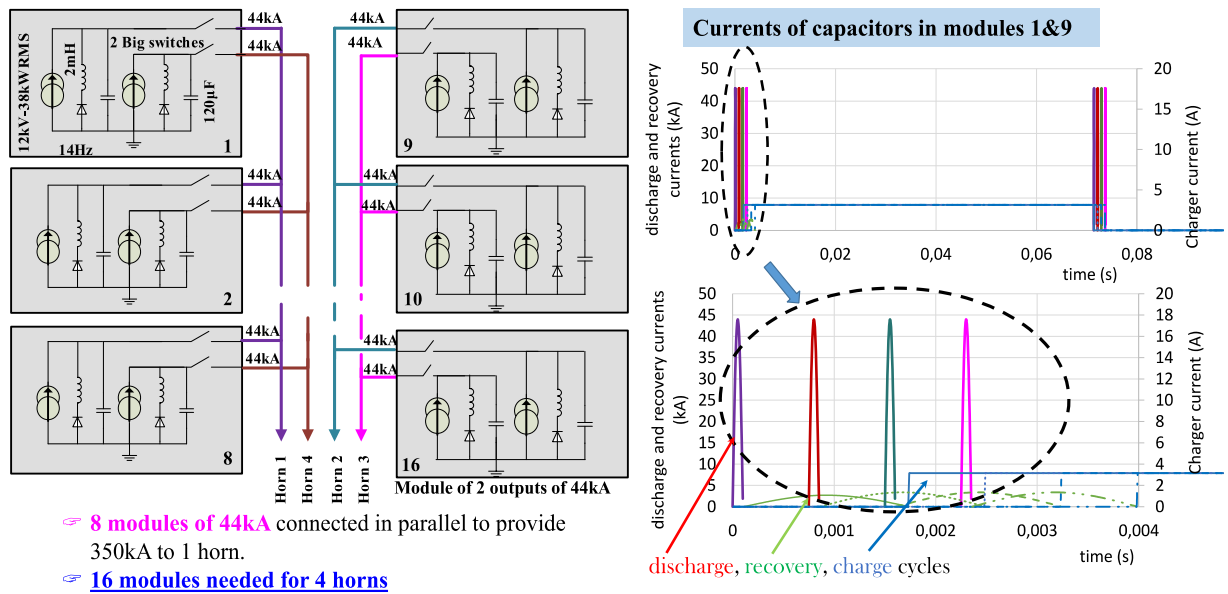

☞ **8 modules of 44kA** connected in parallel to provide 350kA to 1 horn.
☞ **16 modules needed for 4 horns**

Figure 16: Power Supply Principle for option A.

The cost of this solution has been estimated at 5M€.

For option B and C.

The modular approach is able to bring a technically feasible answer to the design of the Power Supply Unit, for the several proton pulse schemes that have been proposed. The solution for scheme A is about 50% more expensive compared to the cost for schemes B and C which is comparable to the EUROν power supply design;

The Horn Power Supply room was relocated outside the Target Station Facility, above the switchyard tunnel, for safety reason and to improve the synchronisation with the Beam Switchyard power supply (Figure 17)**.**
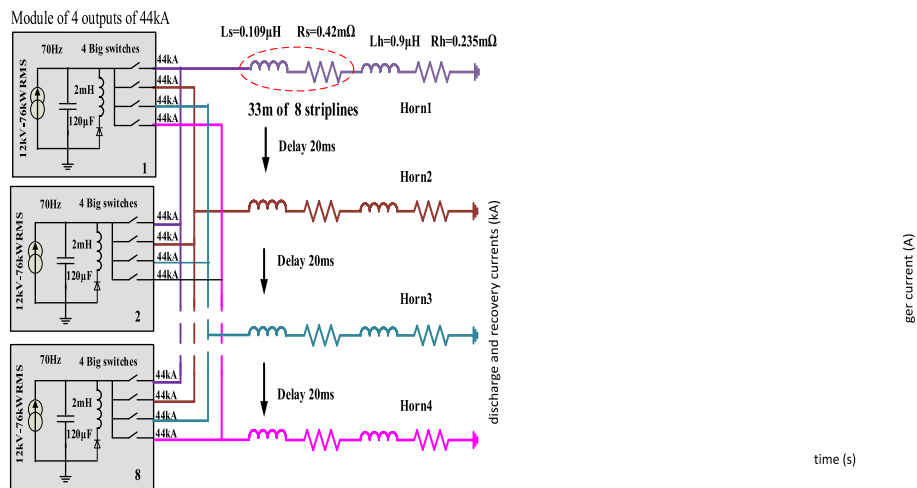

Figure 17: Power Supply Principle for baseline B.

The cost of this solution has been estimated at 3.5 M€.

Alternative hadron collector

The performance of the so-called Los Alamos device used as a hadron collector is being investigated. A crude magnetic field map, computed for the approximate conditions of the ESSνSB, exists. The structure, together with the magnetic field map, were implemented in the particle-matter interaction code FLUKA. The expected pion distribution emerging from the target is used as a particle source in the FLUKA simulation. The neutrino angular and energy distributions at the end of the decay tunnel are extracted. In other words, a complete simulation framework has been setup in the reporting period.

The model used in the FLUKA simulations is a hard-edge model, which implies no variation of the magnetic field in the longitudinal direction. In order to obtain a rough estimate of the ideal structure length, the number of collected neutrinos in the whole energy range as well as in an energy range where the neutrino detection cross section is substantial, was extracted for structure lengths varying from 180

cm to 260 cm. The best collection efficiency occurs at around 220 cm, which is the length used in the remaining simulations.

The neutrino distributions obtained with the Los Alamos field map have been compared with the distribution obtained without any focusing, and with "perfect" focusing. In addition, these distributions are compared with that of the conventional horn in order to assess the performance of the alternative collector, see Figure 18. The first set of results shows that the collection efficiency of the Los Alamos simulation prototype is about half of the collection efficiency of the conventional horn. The expected level of contamination is comparable for the two devices, see Figure 19
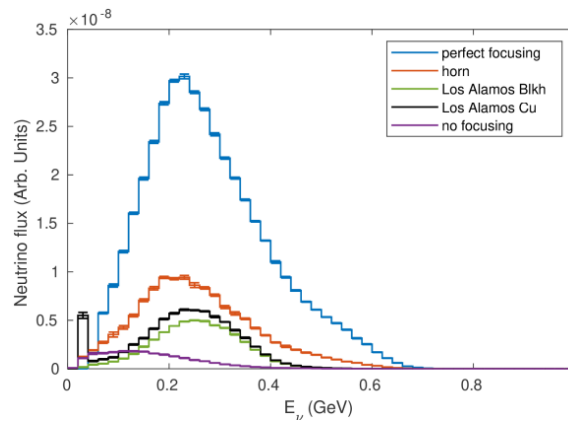

Figure 18: The neutrino flux at 10 km from the source in five cases: perfect focusing, horn, a completely absorbing Los Alamos structure, a Los Alamos structure consisting of copper, and no focusing.
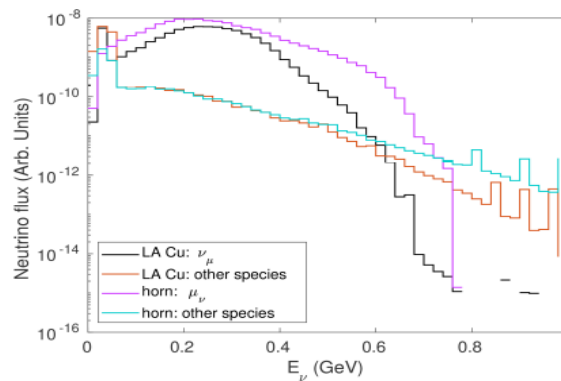

Figure 19: The neutrino flux at 100 km from the source for a 220 cm long Los Alamos device made of copper, compared to that of a horn. The total flux of neutrinos of the wrong species are also shown for the two cases.

Although the conventional horn offers a collection efficiency a factor 2 better than the crude version of the Los Alamos device, the difference is not large enough to fully discard the alternative technology. Therefore, the study will continue.

The studies made so far indicate that the Los Alamos device option will perform better than a superconducting solenoid, moreover performing a neutrino/antineutrino selection. Therefore, from now on the principal effort of this task will be given to this option.

Simulation of the neutrino beam

The method used for the optimization is based on two Monte-Carlo simulations performed with GEANT4 and FLUKA. The results of the simulations are shown in Figure 20 and the beam intensity is detailed in Table 2.
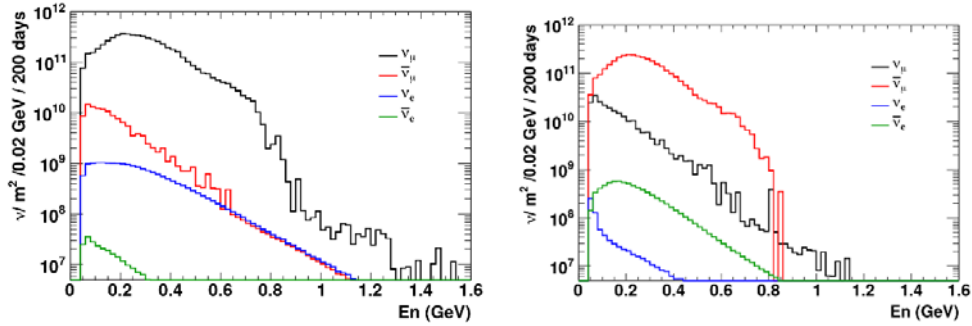

Figure 20: Neutrino fluxes calculated at 100 km distance from the target station for the positive (left panel) and negative polarity (right panel) of the current in the horn.

Table 2: Neutrino flux composition at 100 km distance from the target station.

	Positive		Negative	
	N_ν $(10^{10}/m^2)$	%	N_ν $(10^{10}/m^2)$	%
ν_μ	583	98	23.9	6.55
$\bar{\nu}_\mu$	12.8	2.1	340	93.2
ν_e	1.93	0.3	0.08	0.02
$\bar{\nu}_e$	0.03	0.01	0.78	0.21

The simulation framework has progressed to a new framework using FLUKA software which is commonly used by other experiments to provide the neutrino fluxes, the GEANT4 initial software has progressed in parallel. During this year, the optimisation procedure was able to give the first estimation of the ESSνSB neutrino fluxes.

4. Detector performance

Introduction

The main efforts in the months 13-24 of the project were concentrated on further development of the software for simulation of the near and far detectors and its use to perform such simulations. In this way, we have achieved quite some results. We installed in our framework two simulation/reconstruction codes for water Cherenkov detectors: MEMPHYS and WCSim and developed our own, EsbRoot, based on the best practices of the former two. A simulation package for the fine-grained tracker of the near detector was written. A visualization package was also developed. Global and local coordinate systems were defined and transformations between them calculated and agreed upon.

A first assessment of the Garpenberg and Zinkgruvan mines was done. Under a contract signed with the Division of Mining and Rock Engineering at Lulea University of Technology, Prof. D. Saiang evaluated their suitability from the geological and technical point of view regarding the far detector locations, based on 2D and 3D simulations of various excavation geometries.

Design and performance of the water Cherenkov far detector

In the deliverable _D1.2 Initial facility parameters_ we set as a base-line that the far detector is a water Cherenkov one with around half a megatonne fiducial mass in two water tanks situated in the Garpenberg mine in Sweden, 540 km away from ESS in Lund. Such a detector was simulated within the EUROv Design Study and the results are available (i.e. detection efficiencies, migration matrices, etc., see L. Agostino et.al., _Future large-scale water-Cherenkov detector_, Phys. Rev. STAB, **16,** 061001 (2013)).

We installed the WCSim simulation application and a corresponding reconstruction package, both used by HyperK project. Based on that, we started performing the optimisation of the detector geometry and the coverage of the walls with photo-sensors. We also implemented MEMPHYS geometry into WCSim simulation package and started modifying the reconstruction package accordingly to reconstruct events simulated with WCSim in MEMPHYS geometry.

Figure _21_ illustrates that our EsbRoot framework is capable of simulating neutrino interaction events in the far detector, recording hits in the sensitive elements and event visualisation.
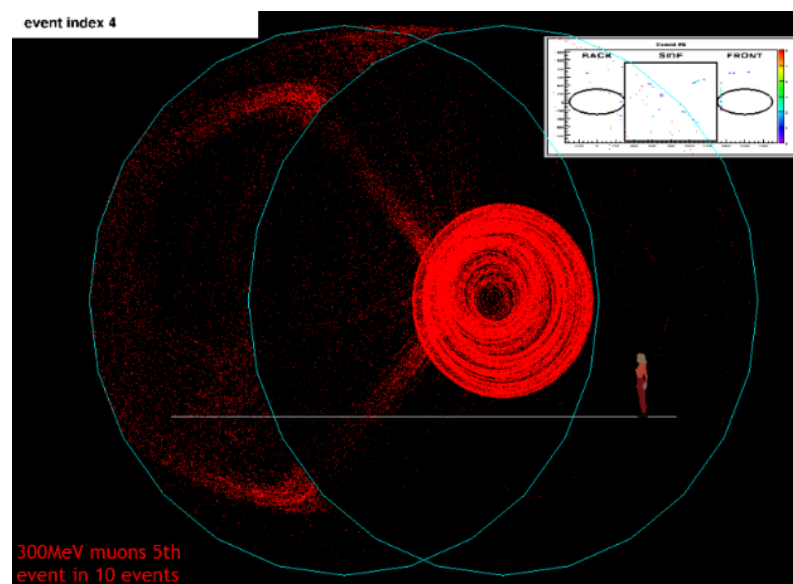

Figure 21: Muon with 300 MeV momentum in the far detector tank

During the reporting period we performed extensive evaluation of the quality of the event reconstruction based on the WCSim + reconstruction packages.

Figure 22 shows preliminary charged lepton momentum reconstruction in the far detector.
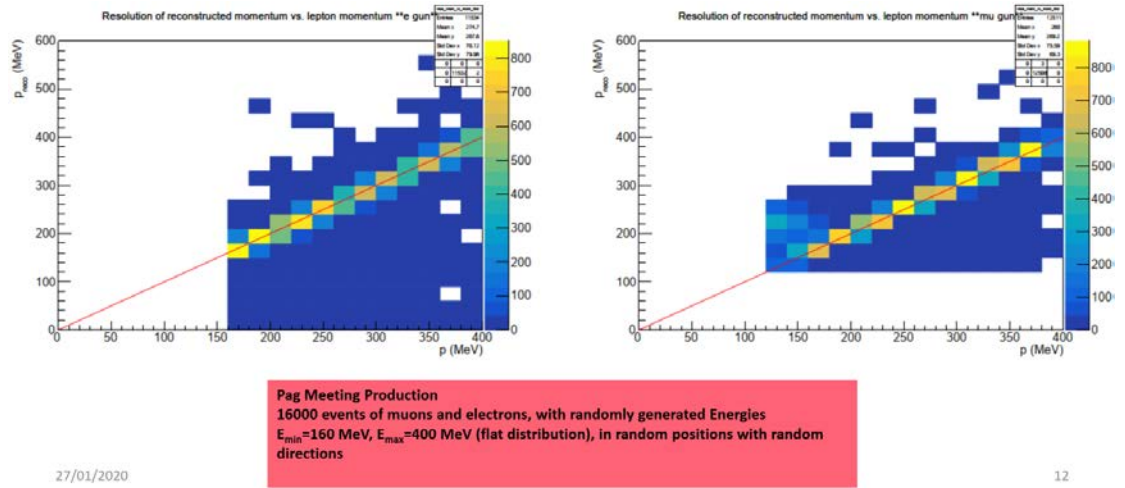

Figure 22: Distributions of reconstructed charged lepton momentum (y-axis) vs. the true simulated one (x-axis), for muons (right) and electrons (left) in the far detector.

Figure 23 demonstrates the preliminary performance of the vertex position reconstruction in the far detector.
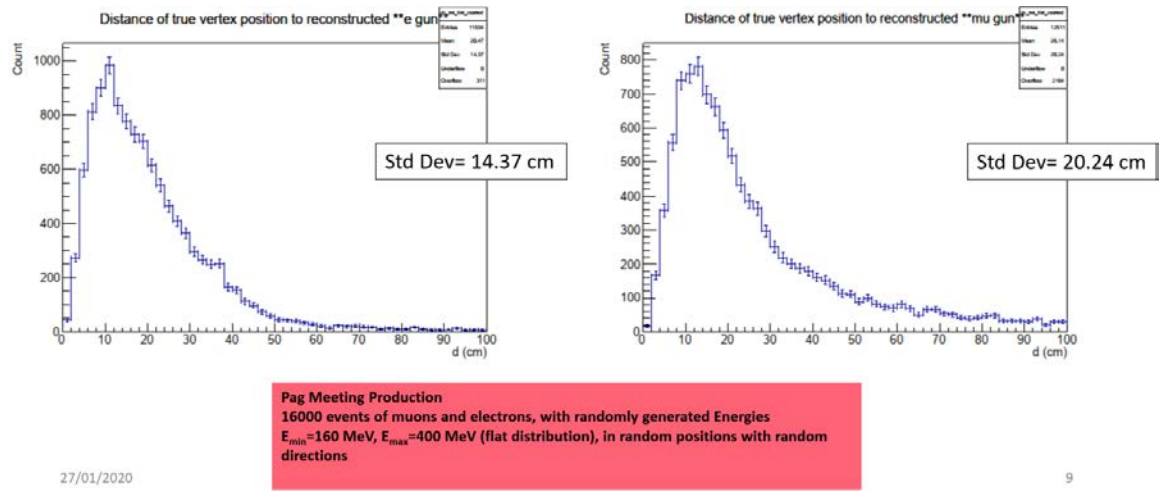

Figure 23: Distribution of the distance between the true and reconstructed vertex position for muons (right) and electrons (left) in the far detector.

Figure 24 demonstrates the performance of the electron and muon identification. It is based on the logarithm of the ratio of maximum values of the likelihood function assuming electron and muon hypotheses. The logarithm should be positive for the electron events and negative for the muon ones.
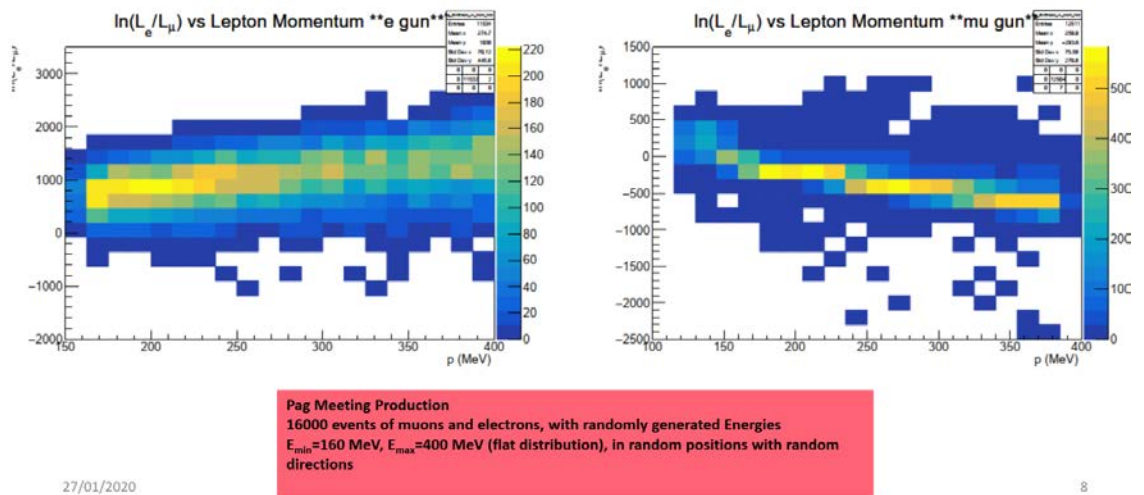
Figure 24: Distribution of the logarithm of the ratio of maximum values of the likelihood function assuming electron and muon hypotheses for true muon events (right) and true electron ones (left).

A working group was set up to evaluate from a geological and technical point of view the suitability of Garpenberg and Zinkgruvan mines in Sweden (and possibly other ones) as a far detector location. This group is composed of two engineers from the Garpenberg mining company Boliden, a local representative of the Hedemora municipality in which Garpenberg is located, and a senior engineer from a local mining consultancy firm. The group is led by David Saiang, an associate professor in mining and rock engineering at Luleå Technical University (LTU) in Sweden. Under a contract signed with the Division of Mining and Rock Engineering at LTU, Prof. D. Saiang wrote a report, based on 2D and 3D simulations of various excavation geometries. The main conclusions of the report are:

- The caverns need to be investigated further in detail. The benchmarking against stopes method[1] in Zinkgruvan gives some guidelines, but the shapes are stopes that are different to the proposed caverns and cannot be correlated directly. The nearest shapes to the proposed caverns are vertical shafts, which have been drilled to over a 1000 m from the ground surface. However, the diameters of the shafts are much smaller. Hence, a more detailed analysis is required, using the shafts as a starting point. Rock reinforcement should be included in the study.

- For both, the Garpenberg and the Zinkgruvan mines, detailed rock mass characterisation is required. This means obtaining information about the body of the rock in which the caverns will be located. The most reliable method to obtain such information is via diamond drilling. Between 270 k€ and 360 k€ will be required for each of the two mines for drilling and analysis of the data.

- The geometry of the caverns should be revised given the boundary conditions of the large horizontal ground stresses and the need to minimise the ratio of the cavern wall surface to the cavern volume.

Based on these studies and a cost minimizing requirement to have minimal wall surface to volume ratio of the tanks, we changed the baseline dimensions of the tanks. The tank diameter will be equal to the tank height, with a dimension of 74 m. That makes a total volume of 310 thousand m^3 for each of the two tanks.

---

[11] The stopes method is based on evaluation of the stability of large excavations called stopes based on their dimensions and rock properties.

Near detector design.

We reviewed the choices made by other accelerator-based neutrino oscillation experiments about their near detectors. Part of the work was done within the COST action CA15139. Based on this review and specific requirements for the ESSvSB near detector we have come to the design described below (see also Design concept of the near detector).

Two different detectors are used and they are coupled together. We have a kiloton mass water Cherenkov detector (WatCh) for event rates measurement and flux normalisation. It will be a lying cylinder of 10 m diameter and 10 m length (total volume 785 m³). A magnetized fine-grained tracker for measurements of poorly known neutrino cross sections in this energy region (60 – 600 MeV) is placed upstream (w.r.t neutrino beam) of the water tank and adjacent to it. The baseline was chosen to be the design developed as an option for the upgrade of the ND280 near detector of the T2K long baseline neutrino oscillation experiment in Japan (see D. Sgalaberna et al., *A fully active fine-grained detector with three readout views, arXiv.org: 1707.01785*). It is called super Fine-Grained Detector (sFGD), and consists of a number of scintillator cubes with dimensions 1x1x1 cm³ each, read out by three-dimensional pattern of wave-length-shifting optical fibres. Our baseline is to use 10^6 cubes that form either a cube with dimensions 1x1x1 m³, or a rectangular cuboid with dimensions 1.4x1.4x0.5 m³. The mass of the tracker will be 1 tonne. When a neutrino interaction happens in the fiducial volume of the tracker, the event topology and momenta of charged particles are reconstructed. Those charged particles that exit the downstream side of the tracker will enter the water volume of the Cherenkov detector where they will be registered and identified. This design is set as a baseline for the near detector (see Figure 25).
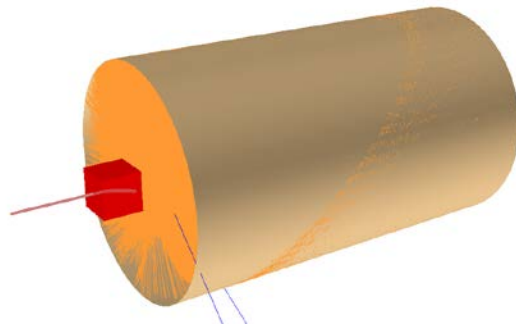

Figure 25: The ESSvSB near detector. The dimensions of the fine-grained tracker in the picture (the red cube) are 1x1x1 m3, while the WatCh cylinder radius is 5 m with the length of 10 m. A magnetic field of 1T is applied in the tracker. The trajectory of a positive muon (red) in the tracker (bended by the magnetic field) and the two neutrinos (blue) from its decay in the WatCh are shown. Emitted Cherenkov photons in the WatCh are shown in orange.

The development and tuning of the software for simulation of particle registration and reconstruction of neutrino events in the WatCh detector is in progress. Along with that, we developed simulation software for the sFGD, including digitization. Reconstruction algorithms are being actively developed and tuned.

A preliminary study was made of the possibility to constrain the initial muon neutrino flux by observing the elastic scattering of neutrinos on electrons in the near detector. This process is well suited for the flux measurement since its cross section can be very precisely calculated from theory. On the other hand,

cross sections for processes in which neutrino scatters off a nucleus are difficult to calculate due to nuclear effects, and there is little data in the energy region of interest for ESSνSB to aid the calculation. The downside of neutrino-electron scattering is that the cross section for this process is by 3-4 orders of magnitude smaller than those for the neutrino-nucleus scattering.

An important step was the integration of the simulation code in the EsbRoot framework. A simulation of the WatCh response to a ν_μ CC interaction done using EsbRoot software framework is presented in Figure 26. Outputs of GENIE, a realistic neutrino interaction generator code, can now be loaded as inputs for the WCSim software event generator for realistic detector design tests, both for the far and the near WatCh detectors.
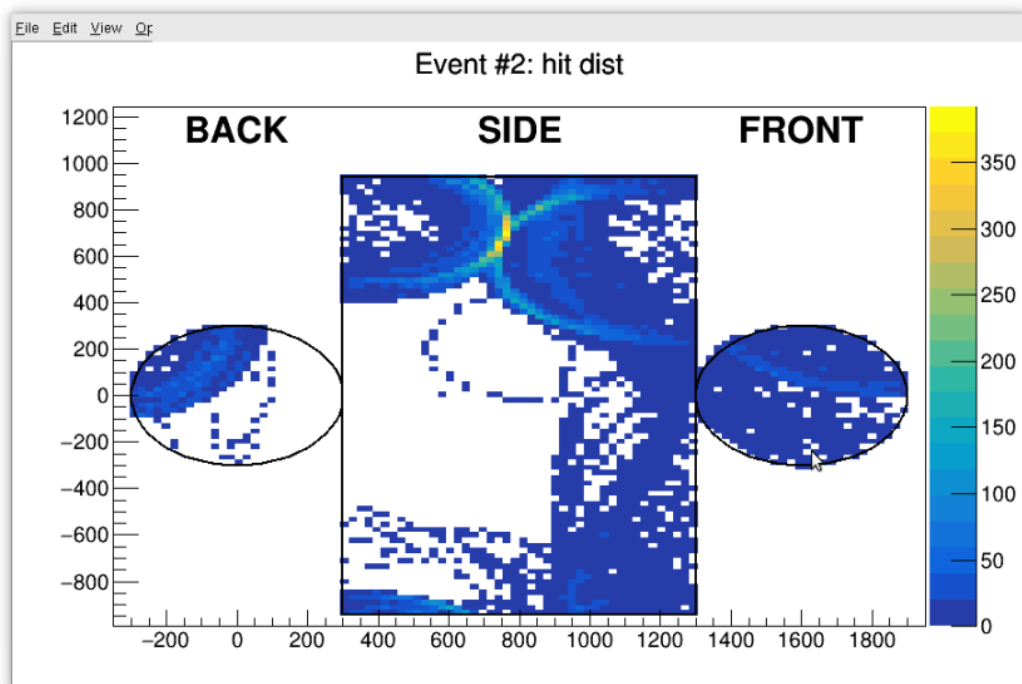

Figure 26: Event display of a simulated ν_μ interaction in the WatCh detector in the EsbRoot framework.

In parallel, the WCSim simulation software twinned with its reconstruction partner are being tuned to simulate and reconstruct neutrino interaction events in the WatCh detector. The reconstruction is based on likelihood calculation for each lepton flavour by using the Cherenkov event topology, specifically the PMT hit charge and time distributions. A preliminary result for energy reconstruction of simulated charged leptons in HyperK WatCh tank scaled down by a factor of 5 is shown in Figure 27.
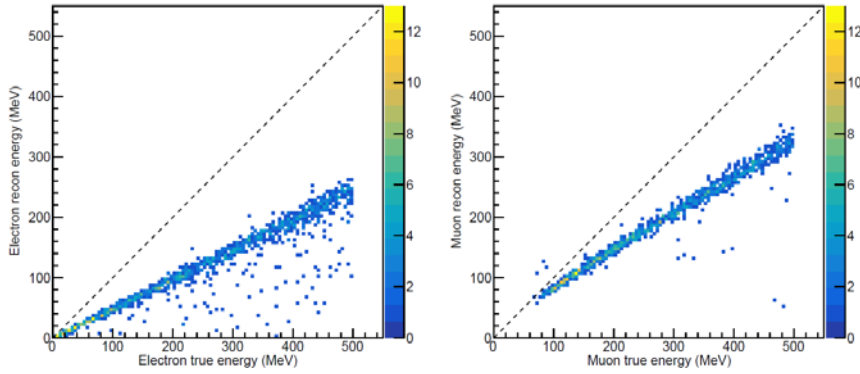
Figure 27: Reconstruction of electron (left) and muon (right) energy in the WatCh detector with scaled down HyperK geometry by factor of 5 in length (10.96 m), radius of the tank (7.08 m), PMT diameter (4 inches) and photo-sensor coverage (40%).

It is seen that dedicated tuning of the reconstruction software is needed. A work in this direction is ongoing, through the use of tuning utility software packages in WCSim which generate the following Monte Carlo sampling output files: Cherenkov light emission profile tables, scattered optical photon tables, charge, angular and time response profiles of the simulated PMTs. These files are necessary in order to provide accurate likelihood probability densities which are tailored to a given WatCh detector geometry. A systematic procedure to generate these files is being developed, which can be applied to the far detector simulation and performance tests in the WCSim framework.

Along with that, we developed simulation software for sFGD type of detector, including digitization. Several pattern recognition reconstruction algorithms are being actively developed, including Hough transformation (from DESY PATHFINDER framework) artificial retina, template matching (from FAIRSHIP), graph traversal (own development) and also track fitting, based on GenFit (http://genfit.sourceforge.net/Main.html).

Also, work on implementation of realistic neutrino flux coming from WP4 is ongoing. The other options being used so far are kept available.

Figure 28 shows the relative difference between the reconstructed and true momentum of the outgoing muons originated from the ESSvSB neutrino beam interactions in the sFGD.
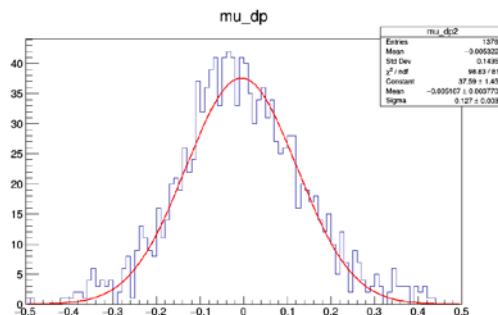

Figure 28: Relative difference between the reconstructed and true momentum of the outgoing muons produced in CC interactions of the ESSvSB neutrino beam in the sFGD. The fit of muon tracks is performed using GenFit package and no pattern recognition is attempted.

Figure 29 shows the relative difference between the true and reconstructed neutrino energy. The calculation assumes CCQE interaction in the sFGD. The neutrino energy is calculated from its kinematical dependence on the outgoing muon momentum. In addition, the proton kinetic energy in sFGD is estimated using the amount of light, produced by it in the scintillator cubes. Then, an attempt is made to obtain the total neutrino energy as a sum of the kinematically calculated one and the proton kinetic energy and the result is shown in the Figure 29. The right tail is due to apparent overestimation of proton energy deposition.
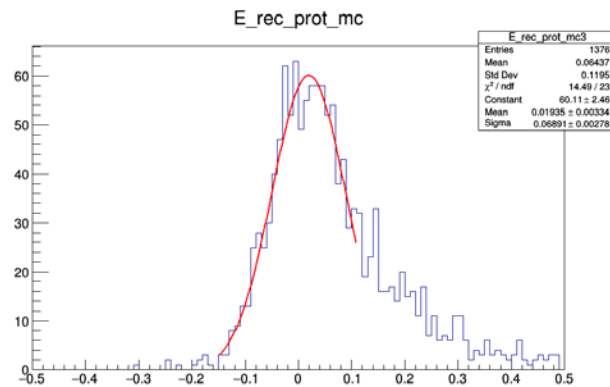

Figure 29: Relative difference between the reconstructed and true muon neutrino energy (see the text for details).

To improve on these preliminary results, further improvement of the reconstruction algorithms is currently under development.

Another important task is the integration of the simulation and reconstruction software for both near sub-detectors (the sFGD and the WatCh) into the EsbRoot framework. This will allow a study of the performance of the whole near detector complex for the measurement of neutrino events. This turned out to be a non-trivial task due to the peculiarities of the WCSim software and the corresponding reconstruction packages. A careful evaluation of the efforts needed and benefits of this integration is under way.

An important achievement of the package is the development of a very versatile and easy-to-use event display, EsbRootView. We owe this to our colleague Guy Barrand. An example of its capabilities is seen in Figure 30.
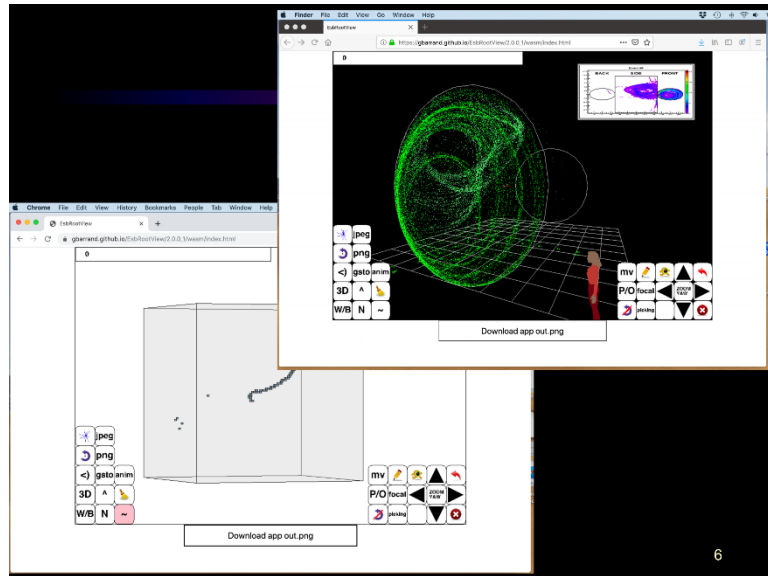
Figure 30: An example of the EsbRootView event display.

Another example is presented in Figure 31, where a neutrino interaction happened in the sFGD with the secondary muon producing Cherenkov light in the near water Cherenkov detector.
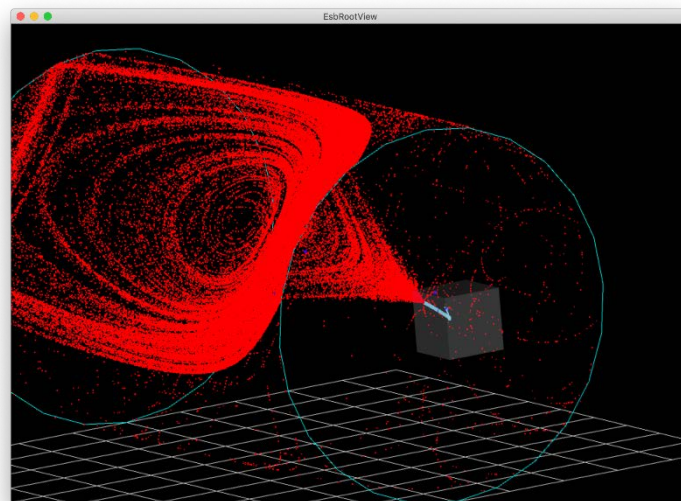

Figure 31: Neutrino interaction in the sFGD cube with the secondary muon producing Cherenkov light in the near water Cherenkov detector.
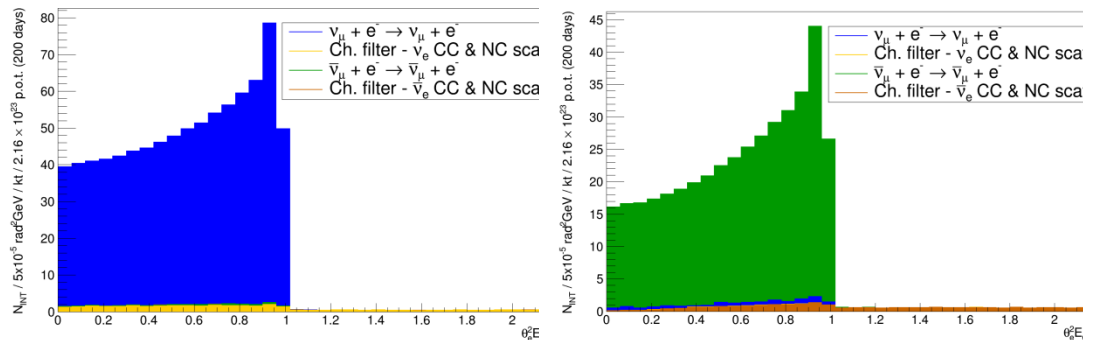
Figure 32: Stacked plots of the distribution of number of expected events vs. Eeθe2 parameter for different processes involving an electron in the final state, for neutrino mode (left) and anti-neutrino mode (right).

To measure the neutrino flux using scattering of neutrinos on electrons, one must discriminate these interactions from ν_e CC induced background. Following the analysis of MINERvA (E. Valencia et al. *Constraint of the MINERvA medium energy neutrino flux using neutrino-electron elastic scattering*. Phys. Rev., D100(9):092001, 2019.), a quantity $E_e\theta_e^2$ (E_e is the energy of the outgoing electron and θ its angle w.r.t. the incoming neutrino) was chosen as a discriminating variable. Using a realistic neutrino spectrum obtained from WP4, it was shown that a good discrimination is possible on a level of true Monte Carlo information. The results are shown in Figure 32.

5. Physics reach

Introduction

The physics reach of the ESSνSB has been updated by combining the observation of the ESSνSB flux tuned for the second maximum of the ν_e appearance probability with the complementary atmospheric neutrino data, more strongly dominated by the first maximum and ν_μ disappearance, and characterized by stronger matter effects. It has been explored how the physics reach of the facility improves when beam data is considered together with the atmospheric neutrino sample. The physics reach and optimization of the ESSνSB facility when combined with the atmospheric data set has been reviewed. It has been studied which sources of systematic errors among the ones considered impact the final sensitivity more significantly.

The simulation of the ESSνSB data has been performed with the GLoBES software [1, 2]. We have assumed that the neutrino beam will shine on a near and a far detector to reduce the systematic uncertainties [3]. The far detector is a 1 Mt MEMPHYS-like water Cherenkov detector [4], while the near detector has been assumed to be identical to the far detector in terms of efficiencies and background rejection capabilities with a fiducial mass of 0.1 kt. The response of the detectors has been implemented through migration matrices, both for the signal efficiency and the background rejection from Ref. [4].

A beam power of 5 MW with 2.5 GeV protons and an exposure of $1.7 \cdot 10^7$ operating seconds per year has been assumed [3]. The fluxes have been simulated explicitly at 1 km from the neutrino target for the near detector [5], accounting for possible geometrical effects since the source cannot be considered point-like, as well as for 100 km (and consequently rescaled) for the longer baselines considered for the far detector [3]. The event rate peaks around O (100) MeV energies, so the dominant contribution to the cross section

will be in the quasi-elastic regime (QE). For the cross section we use the results from the Genie [74] tune G1810a0211a.

We have assumed a total running time of 10 years. Nonetheless, we will also study the dependence of the physics reach on the relative running time spent in positive and negative focusing in order to optimize it for the measurement of CP violation. Likewise, although the preferred location of the far detector for the ESSνSB is the Garpenberg mine at 540 km [3], different baselines, with emphasis in the alternative Zinkgruvan option at 360 km, will be studied to address the optimal choice. Finally, we will also study how the CP discovery potential depends on the total exposure.

Systematics	Opt.	Cons.
Fiducial volume ND	0.2%	0.5%
Fiducial volume FD	1%	2.5%
Flux error ν	5%	7.5%
Flux error $\bar{\nu}$	10%	15%
Neutral current background	5%	7.5%
Cross section $\times$ eff. QE	10%	15%
Ratio ν_e/ν_μ QE	3.5%	11%

Table 1: Conservative "Cons." and optimistic "Opt." values for the systematic uncertainties considered.

Throughout all the simulations we adopt the same treatment of the systematic errors from Table 1 as in Ref. [6]. Unless otherwise specified, we will assume the "Optimistic" systematics from the first "Opt." column in Table 1 although we will also show how the results are affected when the more conservative ones in the second column "Cons." are considered instead.

Correlated systematics between near and far detector will be assumed, uncorrelated between neutrinos and antineutrinos and different flavours. Additionally, to account for the uncertainty in the cross section between the near and far detector, arising from the different flavour composition of the beam (mainly ν_μ in the near site and ν_e for the signal in the far detector), a completely uncorrelated systematic is included for their ratio (last row of Table 1).

We have added to the resulting χ^2 a gaussian prior with the central values and 1 σ errors from Ref. [7] for "solar" and "reactor" parameters. For the "atmospheric" parameters we will set a prior on $\sin^2 2\theta_{23}$ and $|\Delta m^2_{31}|$ given that the octant for θ_{23} and the mass ordering are still unknown. Since the determination of these two parameters comes primarily from atmospherics, when adding this sample to the beam data no prior has been added on θ_{23} and $|\Delta m^2_{31}|$. The simulation of the atmospheric neutrino sample in MEMPHYS is the one used in the analysis from Ref. [8] where the neutrino fluxes at Gran Sasso from **Phys.Rev. D64** calculations [9] were used. This is a conservative estimate as fluxes become larger at higher geomagnetic latitudes such as Garpenberg or Zinkgruvan.
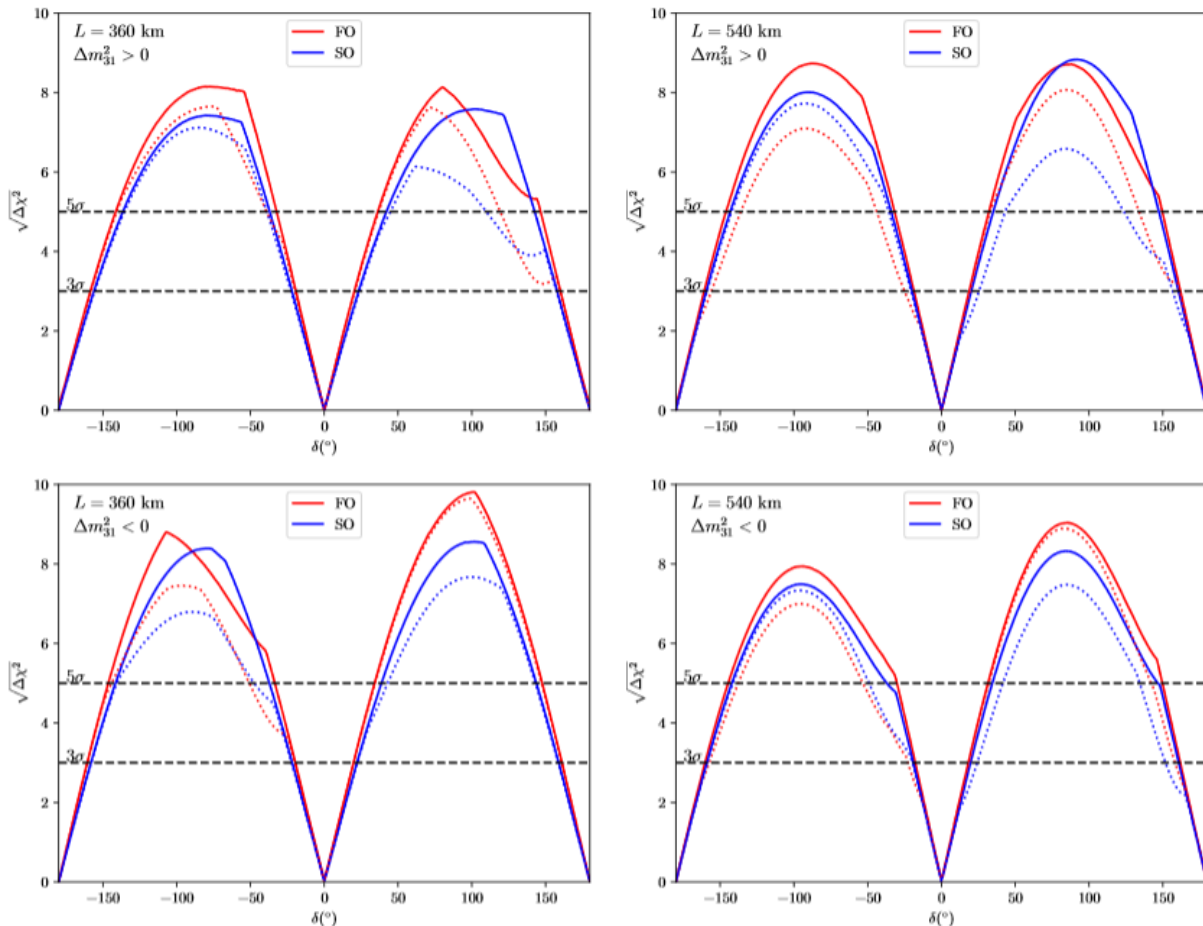
Results

Fig 1: Significance with which CP conserving values of δ can be excluded for the Zinkgruvan 360 km mine (left panels) and Garpenberg 540 km mine (right panels) options. The upper (lower) plots are for normal (inverted) mass hierarchy while the red (blue) curves correspond to θ₂₃ in the first (second) octant. The dashed lines correspond to the beam data only, while the continuous lines correspond to the results studying events from the beam and from atmospheric neutrinos.

In Fig. 1 we show the impact on the CP discovery potential of the ESSνSB before (dashed lines) and after (solid lines) the inclusion of the atmospheric sample for the Zinkgruvan 360 km mine and Garpenberg 540 km mine options in the left and right panels respectively. The plots represent the square root of the $\Delta\chi^2$ with which CP conserving values of δ = 0 or π can be disfavoured as a function of the true value of δ. This can be interpreted as the significance for exclusion of CP-conserving values (and hence evidence for CP violation) as long as the assumptions behind Wilks' theorem hold [10]. Deviations from these assumptions can be sizable for presently running experiments but are expected to be smaller for next generation facilities [11].

Even though the sensitivity of the atmospheric neutrino dataset to δ is almost negligible, the improvement of the ESSνSB physics reach upon its inclusion is quite remarkable. The improvement is generally larger for the longer 540 km baseline than for the Zinkgruvan 360 km option. This is in line with the expectations of the atmospheric sample being more complementary to the beam information at

the longer baseline at which the statistics is significantly lower. Indeed, at the second oscillation maximum the ν_μ disappearance oscillation is not sampled as efficiently as at the first peak and this deteriorates the determination of the atmospheric oscillation parameters θ_{23} and $|\Delta m^2_{31}|$, which plays an important role in the measurement of δ. Conversely, the 360 km baseline has higher statistics and some events also cover the first oscillation maximum so that the atmospheric oscillation information is less complementary and the gain upon its inclusion is less noticeable. From these results we can conclude that the ESSvSB setup combined with the atmospheric neutrino sample would be able to rule out CP-conserving values of δ for ~60% (~55%) of the possible values of δ at the 5 σ level regardless of the octant and the mass hierarchy when observing at the 540 km (360 km) baseline.

Fig. 1 also shows that the gain in CP discovery potential is much more pronounced in some particular regions of the parameter space. Especially for $\delta < 0$ and θ_{23} in the first octant or $\delta > 0$ and the second octant. In these examples the dotted curves for beam only often show a kink that reduces the slope and the values of δ for which CP-violation could be discovered with high significance. Conversely, the corresponding solid curves with atmospheric data either do not display the kink or develop it at higher significance so that the resulting CP-discovery potential is much larger. These kinks occur due to the presence of an unresolved octant degeneracy at a CP-conserving value of δ that prevents drawing conclusions regarding CP violation. When atmospheric data is added, the sensitivity to the octant improves and these degeneracies are either lifted or only show up at much higher significance.
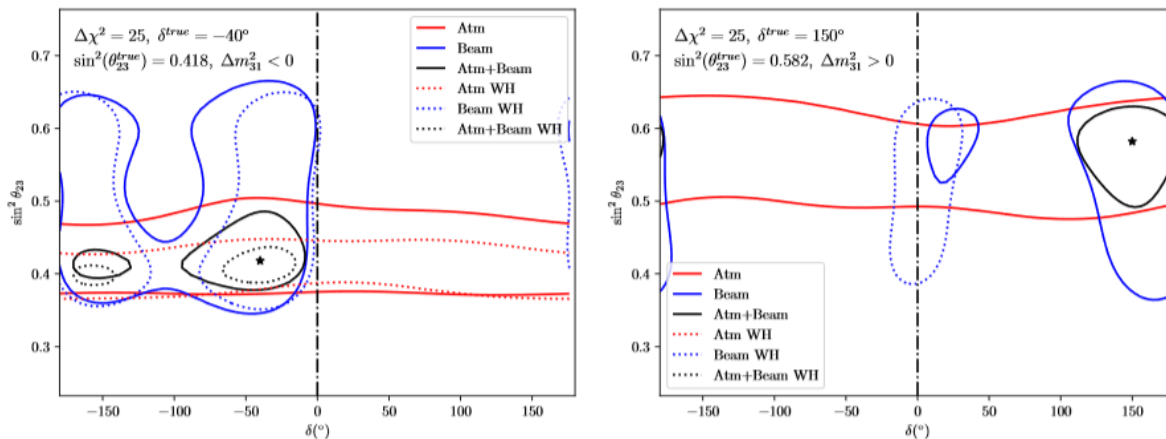

Fig 2: Allowed regions at $\Delta\chi^2 = 25$ for different assumed values of $\sin^2\theta_{23}$ and δ represented by the star for a 540 km baseline (Garpenberg location). The red curves correspond to the atmospheric dataset alone, the blue to the beam-only information and the black curves to the combination of both. Dotted regions are allowed with the wrong mass hierarchy.

This situation is illustrated in Fig. 2, where the allowed regions at the $\Delta\chi 2 = 25$ level (5σ if the assumptions behind Wilks' theorem are satisfied) are shown in the δ-$\sin^2\theta_{23}$ plane. The left (right) panels assume the true values $\delta = -40^\circ$ ($\delta = 150^\circ$), $\sin^2\theta_{23} = 0.418$ ($\sin^2\theta_{23} = 0.582$) and normal hierarchy. As can be seen, when only the beam information is taken into account (blue curves), an octant degeneracy that spreads the allowed 5σ region towards CP conserving values appears. Conversely, the atmospheric data on their own (red curves) have no capability to determine δ at all, but can instead rule out the wrong octant of θ_{23}. Thus, the combination of the two data sets (black curves) very significantly improves the CP discovery potential of the facility in these areas of parameter space. The dotted lines correspond to "sign" degeneracies with the opposite mass hierarchy to the one chosen as true value. In the right panel, this degeneracy is also solved with atmospheric data while for the values of δ and θ_{23} chosen in the left panel a small sign degeneracy remains between the 4 and 5σ level. Notice that an "intrinsic degeneracy" at $\delta' = \pi - \delta_{true}$ also shows up at the 5σ level when only the beam information is taken into account. As for the

"sign" degeneracy, the atmospheric neutrino data is enough to lift it for the parameters chosen in the right panel while a small remnant is present in the left. In any case, both the "intrinsic" and the "sign" degeneracies appear at $\delta' = \pi - \delta_{\text{true}}$ given the comparatively small matter effects for the setup. Their allowed regions are smaller or comparable to that of the true solution so that only the "octant" degeneracy plays a significant role in reducing the CP-discovery potential when atmospheric data is not exploited to lift it.
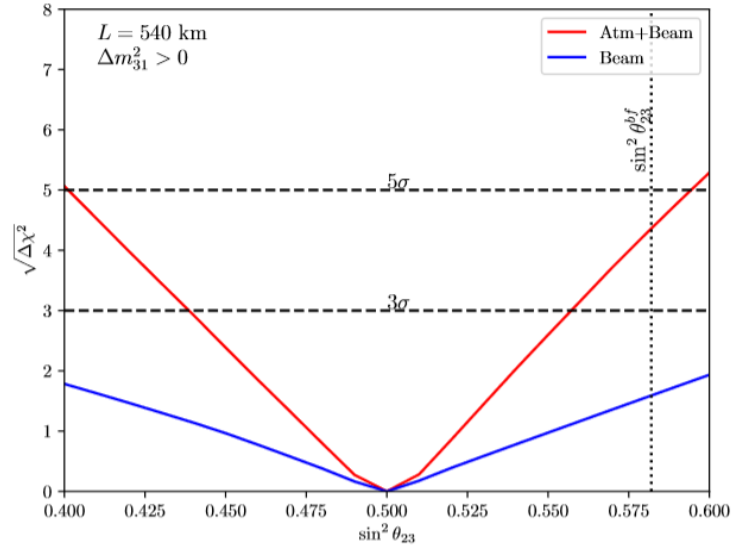

Fig 3: Significance with which the wrong octant would be disfavoured as a function of the actual value of θ_{23} with beam-only information (blue lines) and including also the atmospheric dataset (red lines) for the baseline to Garpenberg (L= 540 km) and normal mass ordering. The results for the Zinkgruvan site (L= 360 km) and for inverted ordering are very similar. The vertical line represents the present best fit for θ_{23} from [7].

In Fig. 3 we show how the significance with which the ESSνSB would be able to disfavour the wrong octant of θ_{23} as a function of the true value of θ_{23} (blue lines). As already anticipated this capability improves dramatically upon the inclusion of the atmospheric neutrino sample (red lines) and thus the potentially dangerous "octant" degeneracies are lifted. The curves are almost identical for both mass orderings and for the Zinkgruvan and Garpenberg baselines.

The significance with which the ESSνSB would be able to disfavour the wrong mass ordering is shown in Fig. 4, where dotted (solid) lines correspond to beam only data (beam and atmospheric data). The left (right) panels correspond to the 360 km (540 km) baseline and upper (lower) panels are for the scenario in which the true hierarchy is normal (inverted). As can be seen the ESSνSB beam data allows to disfavour the wrong mass ordering at around the 3σ (2σ) level for the 360 km (540 km) baseline for any value of δ and the octant. When the atmospheric data is added, the sensitivity to the wrong hierarchy is boosted to the 4-5σ level or even higher for the particular case of normal hierarchy and second octant of θ23 (sin²θ23= 0.582 from Ref. [7]) for which the signal in atmospheric neutrinos is enhanced.
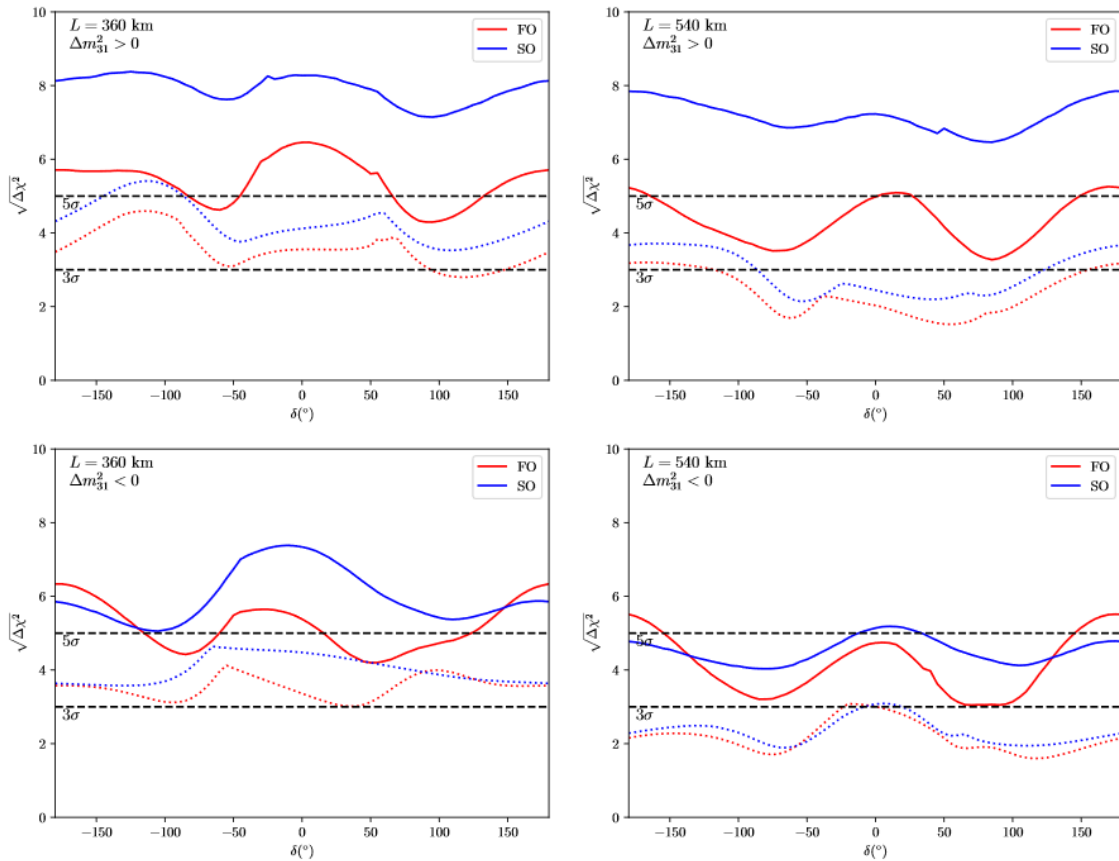
Fig 4: Significance with which the wrong mass ordering would be disfavoured for θ₂₃ in the first octant (red lines) or second octant (blue lines) and the true mass ordering being normal (upper plots) or inverted (lower plots). Dashed lines correspond to the beam only data while solid lines correspond to the addition of the atmospheric sample. The left panels correspond to the baseline of Zinkgruvan while the right ones to the location of the Garpenberg mine.

In Fig. 5 we analyse the precision with which the ESSvSB experiment would be able to measure the CP-violating phase δ. In this figure, we assumed the currently preferred option of normal ordering and second octant of θ23. In the upper panels we show the improvement in the 1σ allowed region with which δ would be constrained by adding the atmospheric neutrino sample (solid lines) to the beam information alone (dotted lines). As can be seen, both for the 360 km (left panel) and 540 km baseline (right panel), the precision with which δ could be determined has a very pronounced shape. For CP violating values of δ around ± 90º, we obtain the worst precision and the 1σ uncertainty in the measurement peaks, while for δ around 0 or 180º the best precision is obtained. As discussed in Ref. [12], this structure follows from the dependence of the oscillation probability on δ. At an oscillation peak $|\Delta m^2_{31}|L/(4E) = (2n-1)\pi/2$ and thus mainly sinδ is probed. Since the derivative of sinδ vanishes at δ=±90º, the precision with which δ can be determined is worse close to these values. In order to constrain δ around δ=±90º, measurements away from the oscillation maxima to determine cosδ would instead be necessary. These off-peak measurements are easier at the Zinkgruvan 360 km baseline since the statistics is higher and also the beam is not exactly centred at the maximum, while they are very challenging at Garpenberg since very few events away from the oscillation peak are expected. This explains why the reconstructed sensitivities around δ = ±90. are much worse in the right panel compared to the left ones. Moreover, the double-peak structure that can be seen for δ = −90º for 540 km corresponds to the "intrinsic" degeneracies depicted in Fig. 2 that merge into one bigger allowed region. Since, as seen in Fig. 2, the addition of atmospheric data can lift these degeneracies, in the solid lines where this information was included the difference

between the two baselines is significantly reduced. Conversely, for δ= 0 or 180º the measurement on peak is what allows to determine δ and, since this is better covered at the longer 540 km baseline, the precision is slightly better there. This fact also translates into the better CP-discovery potential observed for the 540 km baseline in Fig. 1. Since the error in δ is smaller around CP-conserving values, the 540 km option allows getting closer to CP conservation and still be able to claim the discovery of CP violation at high significance.
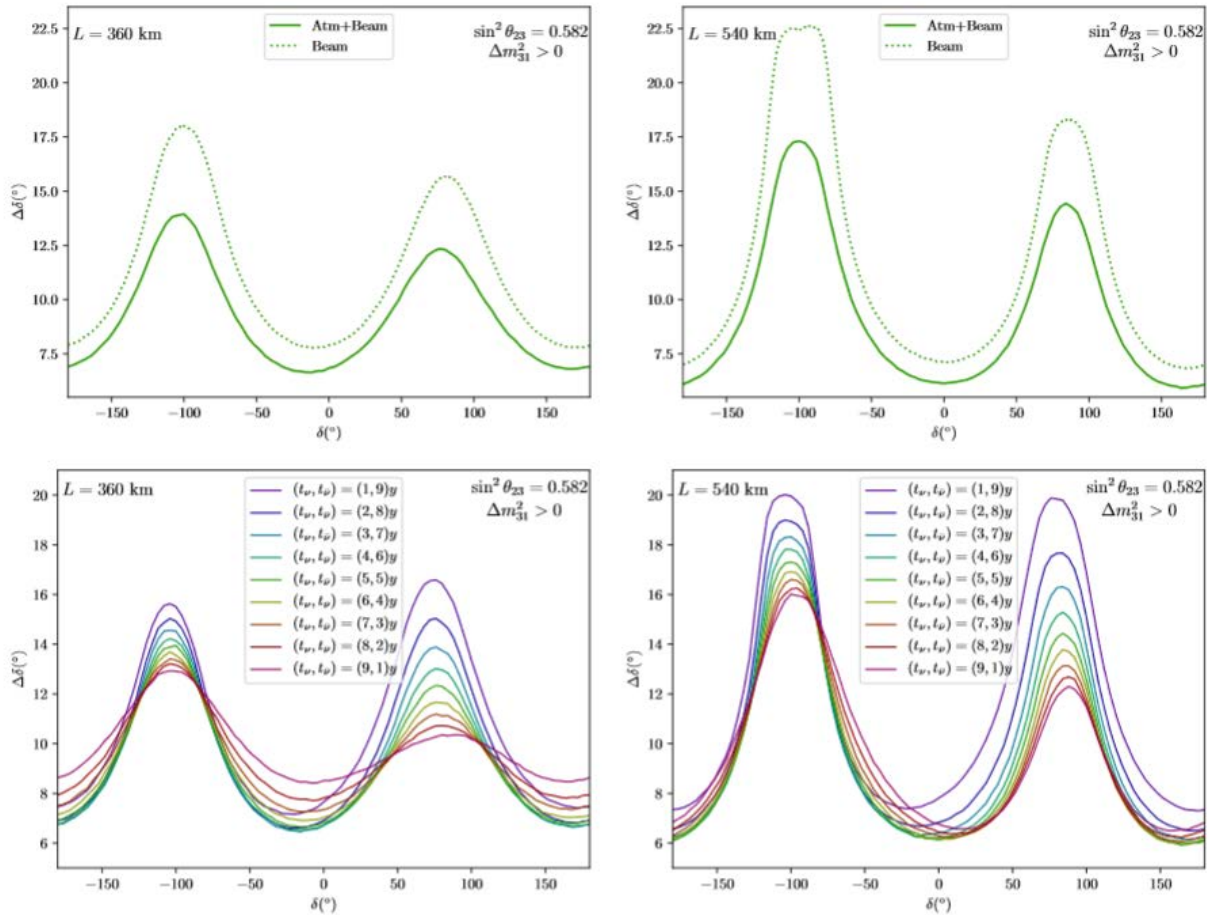

Fig 5: Precision (spread of the 1σ allowed region) on the determination of δ for the baseline to Zinkgruvan L = 360 km (left panels) and Garpenberg L = 540 km (right panels) for the current best-fit parameters [21]. In the upper panels, we show the comparison between the precision obtained with (solid lines) and without (dashed lines) the atmospheric sample for a running time of 5 years in each focusing. In the lower plots, we show the dependence of the precision on the relative running time in each mode, where t_ν ($\bar{t}_\nu$) corresponds to the time the experiment would run in neutrino (antineutrino) mode, combining atmospheric and beam datasets.

In the lower panels of Fig. 5, the impact of changing the relative running times in positive focusing (neutrino mode) and negative focusing (antineutrino mode) is shown. Since off-peak measurements are required for δ = ±90º, statistics are crucial and easier to accumulate in neutrino mode, where fluxes and cross sections are higher and so the best precision would be obtained by devoting longer periods of data taking to positive focusing. Conversely, around δ = 0 or 180º the complementarity between the neutrino and antineutrino samples pays off and more even splits of the running time provide better sensitivity.

Since the ESSνSB would be a next-generation Super Beam neutrino facility, its measurement strategy can profit from the previous hints by preceding oscillation experiments and adapt the splitting between neutrino and antineutrino modes depending on what value of δ data points to. If such a strategy is

followed and the best splitting between neutrino and antineutrino modes is adopted for each value of δ, the precision presented in Fig. 6 would be obtained. If the mass hierarchy is confirmed to be normal and θ23 lies in the second octant as present data prefer, the precision with which the ESSνSB facility would determine δ ranges from 16º (13º) for δ∼−90º to 6º (7º) for δ∼0 or δ∼180º for 540 km (360 km).
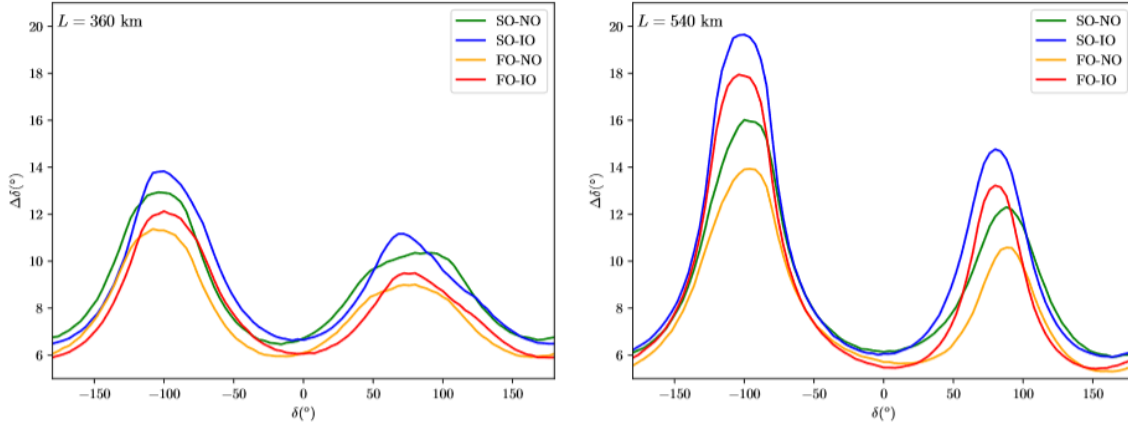

Fig 6: Precision on the measurement of δ for a total running time of 10 years when the relative running time in neutrino and antineutrino modes is optimized for each value of δ. This corresponds to running similar times in neutrino and antineutrino modes around δ= 0, 180º and maximizing the neutrino runs around δ=±90º.

From Figs. 1 and 6 one can conclude that if the experiments preceding the ESSνSB do not find any evidence of CP-violation, the best option would be the 540 km baseline and a more or less even split of the neutrino and antineutrino running times. Indeed, this choice would minimize the errors with which δ would be determined around CP-conserving values and allow to increase the CP-discovery potential. On the other hand, if the previous set of experiments determine δ to be close to maximally CP-violating, then the best scenario for the ESSνSB would be the shorter 360 km baseline and increased neutrino run time to determine δ with the best precision possible.
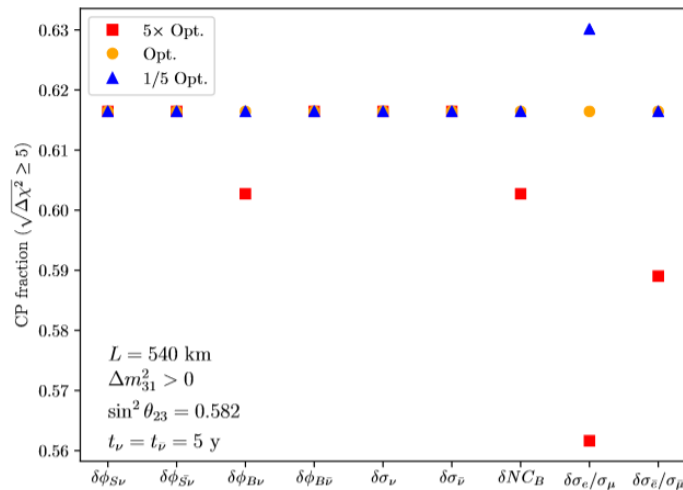

Fig 7: Impact of different sources of systematic errors on the fraction of values of δ for which a Δχ²>25 exclusion of CP conservation would be possible at the Garpenberg mine. The orange circles correspond to the CP fraction with the "Optimistic" systematics from Table 1, red squares correspond to assuming that particular uncertainty to be 5 times larger and blue triangles to reducing the uncertainty by a factor of 5.

In Fig. 7 we show the impact of individual systematic uncertainties on the final fraction of values of δ for which CP violation could be discovered (Δχ² ≥ 25). The sources of uncertainty considered, summarized in Table 1, are the flux uncertainties for the signal (δφ$_S$) and background (δφ$_B$), the cross section systematic (δσ), the neutral current background (δNCB), and the uncertainty on the ratio of the electron and muon flavour neutrino cross section (δσe/σµ). The plot shows that the systematic uncertainties that most significantly affect the performance of the ESSνSB are the ones related to the background components of the beam, since for these the determination at the near detector is more challenging. Namely, δφ$_B$, δNCB as well as δσe/σµ since the only νe present at the near detector that would allow to fix this parameter are those from the intrinsic background contamination of the beam. Among these, the strongest impact on the sensitivity is due to the cross-section ratio since, not only it is difficult to constrain, but it is also most relevant to the signal at the far detector, which consists of νe. Indeed, reducing or increasing this particular source of systematic error has the biggest impact on the physics reach. The impact is in any event limited, since the main bottleneck to the performance when observing at the second oscillation peak is statistics. In particular, a reduction of this systematic by a factor of 5 improves the CP fraction by ∼2% (no impact for antineutrinos) while the same factor in the opposite direction worsens the sensitivity by ∼9% (∼4%).
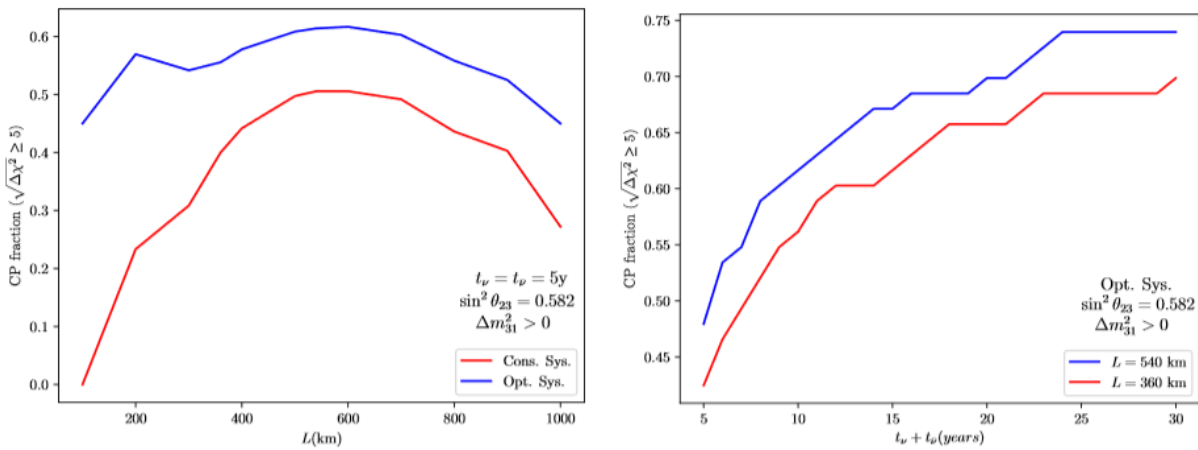

Fig 8: Fraction of values of δ for which CP violation could be discovered above 5σ for different baselines to the far detector (left panel) for the two different sets of systematics from Table 1. In the right panel, we show the CP fraction for the Garpenberg (L= 540 km) and Zinkgruvan (L= 360 km) mines, assuming the current best fit values for the oscillation parameters and the "Optimistic" systematics for increasing total exposure.

The importance of these systematic errors in the physics reach is crucially dependent on the baseline of the experiment. In the left panel of Fig. 8 we show the fraction of all the possible values of δ for which it would be possible to rule out δ= 0 or δ= 180º with a Δχ²= 25 or higher significance. The upper blue line is for the more optimistic systematics from Table 1 and the lower red one for the more conservative values. As can be seen, the fraction of values of δ at which a 5σ discovery would be possible, peaks between 400 km and 700 km in both cases. But this peak is much more pronounced when the more conservative values are assumed for the systematic uncertainties. Indeed, for larger values of the systematics, the shorter baselines are strongly penalized since the dependence of the oscillation probability is sub-leading around the first peak and easily hidden by the systematics. Conversely, if small systematic errors can be achieved, then the main limiting factor would be statistics and shorter baselines would perform better. Thus, by measuring at the second oscillation maximum the ESSνSB setup becomes much more resilient to sources of systematic errors unaccounted for when observing only at the first peak.

In the right panel of Fig. 8 we show how the fraction of values of δ for which CP violation would be discovered at the 5σ level by the ESSνSB beam and atmospheric data increases with the exposure. As

expected from an observation at the second oscillation peak, statistics is the main factor controlling the final reach of the experiment. Indeed, for 5 years data taking the CP fraction is around 46%, by 10 years it increases to 62% and reaches 70% for 20 years of exposure. The slope only flattens significantly after 25 years.

Sensitivity to Light Sterile Neutrinos

In this section, we will discuss the sensitivity of the ESSvSB experiment to light sterile neutrinos. Sterile neutrinos are SU(2) singlets, which do not interact with the Standard Model particles, but they can mix with active neutrinos and therefore take part in the phenomenon of neutrino oscillations. For a review on the subject of light sterile neutrinos, see Ref. [13]. We perform and present our results for 5 years running in neutrino mode and 5 years running in antineutrino mode. The results assume normal neutrino mass ordering.
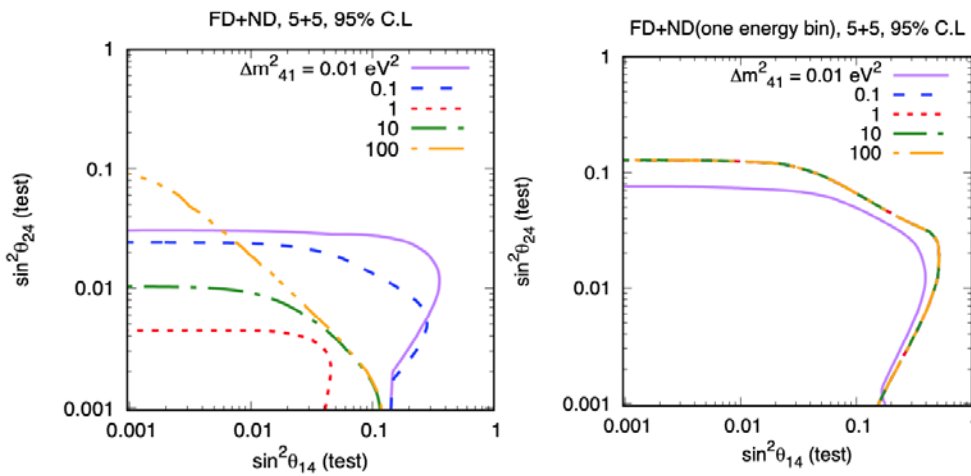

Fig 9: Sensitivity to sterile neutrino in the $\sin^2\theta_{14}$ vs $\sin^2\theta_{24}$ plane for different values of Δm^2_{41}.

In Fig. 9, we present the capability of ESSvSB to constrain the sterile neutrino parameters in the $\sin^2\theta_{14}$ vs $\sin^2\theta_{24}$ plane for different values of Δm^2_{41}. In the left panel, we show the results for the combination of far detector (FD) and near detector (ND), and in the right panel, in order to estimate the sensitivity for the FD without any ND, we show the results for a detector configuration of FD+ND without any energy information on the ND. In other words, we consider only one energy bin for the ND. Therefore, in these panels, the ND just acts as a counting experiment. We adopt this method so that the systematic uncertainties in the FD+ND and only an FD without any ND remain comparable. We see that for Δm^2_{41} = 0.01 eV^2, the bounds are weak as for this value of Δm^2_{41}, the oscillations have not yet developed for the ND and the sensitivity comes from the FD. Increasing the value of Δm^2_{41}, the oscillations become more developed in the ND and we obtain the best bound for Δm^2_{41} = 1 eV^2. This is because for this value of Δm^2_{41} the oscillations are fully developed at the ND. Increasing the value of Δm^2_{41} further, the oscillations tend to become rapid and again the sensitivity decreases. From the right panel, we note that when there is no spectral information on the ND, the sensitivity for Δm^2_{41} = 1 eV^2 is lost and for all values of Δm^2_{41} we obtain similar sensitivities. This is because now the sensitivity comes from the FD, where the oscillations due to the sterile neutrinos are averaged out and the sensitivity due to different values of Δm^2_{41} is lost. From the plots, we note that the bounds on θ_{24} are slightly better than the bounds on θ_{14}. This is because the sensitivity to θ_{24} comes from both the appearance and the disappearance channels, whereas the sensitivity to θ_{14} comes only from the appearance channel.

In Fig. 10, we present the sensitivity to sterile neutrinos that could explain the electron neutrino appearance in the former LSND experiment. As can be observed, at short baseline lengths that could be probed by the ND, the sensitivity to this region of parameter space is very good. This is due to the fact that at the ND the shape of the event rate with sterile neutrinos cannot be mimicked by overall systematics (red curve), and thus, the sensitivity to the mixing is at the order of 10^{-4}. If there was no energy information in the ND (purple curve), we observe that the sensitivity drops dramatically for the interesting region of neutrino mass-squared differences, to the level of the systematics.
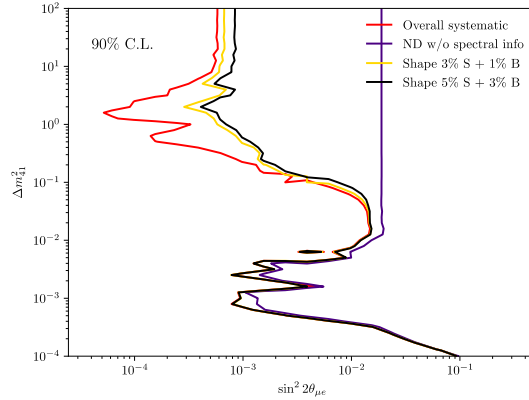

Fig 10: Sensitivity to the sterile neutrino mixing parameters of interest necessary to explain the LSND anomaly for different choices of systematic errors. The red curve corresponds to having only overall systematics, the purple one accounts to having no spectral information in the near detector, while the golden and black curves correspond to including different levels of shape systematics.

An interesting study is to introduce systematic uncertainties that depend on the energy and therefore introduce shape systematics (golden and black curves). These uncertainties could arise from the cross section or the neutrino flux that are better known at some energies than others and can hide the effect of sterile neutrinos in the ND. As can be seen in Fig. 10 (with just 3 % in signal and 1 % shape systematics in the background), the sensitivity to sterile neutrinos drops an order of magnitude in the effective mixing angle. Therefore, a very precise control of this kind of systematic uncertainties is needed in order to probe the parameter space interesting for LSND [14], which is around $\Delta m^2_{41} = 1$ eV^2.
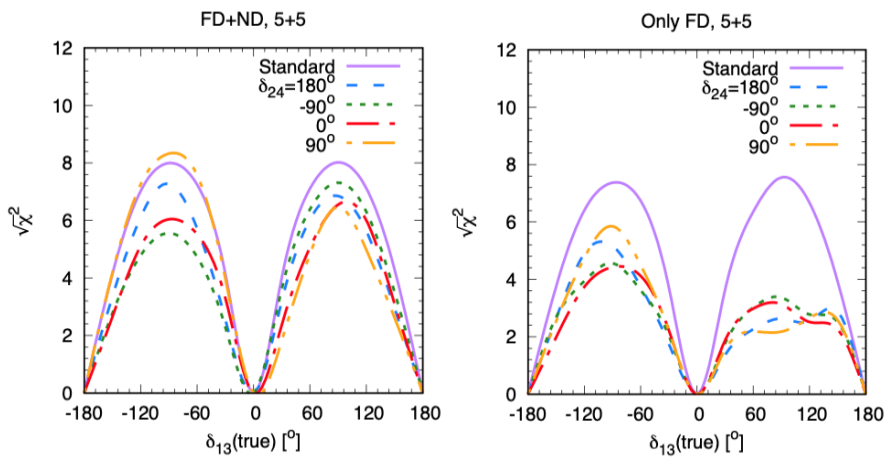

Fig 11: Sensitivity CP violation sensitivity due to the standard Dirac phase δ_{13} in presence of a light sterile neutrino having $\Delta m^2_{41} = 1$ eV^2.

In Fig. 11, we present the CP violation sensitivity of ESSvSB assuming the existence of a light sterile neutrino having Δm^2_{41} = 1 eV^2. In the left panel, we show the sensitivity for FD+ND, and in right panel, we show the sensitivities for only a FD with 8 % (10 %) overall systematics in signal (background). From these figures, we see that when there is no ND, the CP violation sensitivity in the presence of sterile neutrinos is lower as compared to the case when we include an ND along with an FD. This is because when we include the ND, the sterile mixing parameters are constrained due to the oscillations of the sterile neutrinos at the ND, which is not the case for only an FD, where the oscillations of the sterile neutrinos are averaged out and the constraints on the sterile mixing parameters are weaker. We have checked that for the case of only an FD, the sensitivity is affected due the marginalization of θ_{14}. For the combined FD and ND, we note an asymmetry in the curve for δ_{24} = -90º and 90º. For δ_{24} = -90º (90º), we see that the sensitivity is higher around δ_{13} = 90º (-90º). We have checked that this happens due to the marginalization of θ_{24}. The results in the right panel of Fig. 11 are comparable with the results given in Ref. [15]. However, the conclusion drawn in Ref. [14] that the CP violation sensitivity deteriorates substantially in the presence of sterile neutrinos can be altered if the experimental setup includes a ND.

Scientific publications and Talks and Posters presented at International Conferences and Workshops

Scientific publication related to the Linac, Accumulator, Target and Detectors sections

1. **ESSνSB Target and Horn Studies and Future Development** E. Baussan. *Proc 20th International Workshop on Neutrinos (Nufact2018), 12-18 August, Blacksburg, Virginia.* (published in 2019) DOI: 10.22323/1.341.0110.
2. **Upgrade possibility of the ESS linac for the ESSvSB project**, B. Gålnander, M. Eshraqi and A. Farricker, *(Nufact18)*, 12-18 August, Blacksburg, Virginia (published in 2019) DOI: 10.22323/1.341.0115
3. **The European Spallation Source Neutrino Super Beam Design Study**, M. Dracos and al, Proc. *10th Particle Accelerator Conf. IPAC'19, Melbourne, Australia 19 May 2019*. DOI: 10.18429/JACoW-IPAC2019-MOPRB004.
4. **Status of the ESSvSB Accumulator Design.** M. Eshraqi and al. P*roc. 10th Particle Accelerator Conf. IPAC'19, Melbourne, Australia 19 May 2019.* p. 666-668 DOI: jacow-ipac2019-moprb046. A paper for the conference proceedings has been submitted. Title: Challenges and Status of the ESSvSB accumulator design, Ye Zou.
5. **Status of ESS Linac Upgrade Studies for ESSvSB**. B. Gålnander, M. Eshraqi, C. Martins, R. Miyamoto, A. Farricker and M. Collins, proceedings of IPAC 2019.Talks in International Conferences and Workshops for WP2 during the reporting period. DOI: 10.18429/JACoW-IPAC2019-MOPTS082
6. **ESSvSB Target Station.** E. Baussan and al. *Proc. 10th Particle Accelerator Conf. IPAC'19, Melbourne, Australia 19 May 2019*. DOI: 10.18429/jacow-ipac2019-thprb013.
7. **Proton decay at one loop**. J. C. Helo, M. Hirsch, T. Ota. Published in Phys.Rev. D99 (2019) DOI: 10.1103/PhysRevD.99.095021
8. **Neutrino Portals to Dark matter**. M. Blennow, E. Fernandez-Martinez, A. Olivares-Del Campo, S. Pascoli, S. Rosauro-Alcaraz, A.V. Titov. Feb 28, 2019. Published in Eur.Phys.J. C79 (2019) no.7, 555. DOI: 10.1140/epjc/s10052-019-7060-5
9. **Physics Potential of ESSvSB.** M.Blennow, E. Fernandez-Martinez, T Ota, S. Rosauro-Alcaraz. Published in the European Physical Journal C. DOI : 10.1140/epjc/s10052-020-7761-9
10. **A comparative study between ESSvSB and T2HK in determining the leptonic CP phase.** M. Ghosh and T. Ohlsson, preprint: arXiv:1906.05779 [hep-ph]. DOI: 10.1142/S0217732320500583
11. **The accumulator ring for the ESSvSB project - a progress report**, Ye Zou. Submitted to Proceedings of The 21st International Workshop on Neutrinos from Accelerators (NUFACT2019).
12. **Status of the detector design studies for ESSvSB**, J.Parc and al. The 21st international workshop on neutrinos from accelerators (NuFact2019), Proceedings of Science (submitted).
13. **ESSvSB – and deltaCP**, J. Cederkall with the ESSvSB collaboration, European Physical Society Conference on High Energy Physics (EPS-HEP2019), Proceedings of Science (submitted).

Talks in International Conferences and Workshops

1. The Neutron European Spallation Source and the proposed neutrino Super Beam for CP Violation discovery was presented at the *Conference on Recent Developments in High Energy Physics and Cosmology (HEP 2019),* 17TH April 2019, Athens, Greece, Marcos Dracos.
2. The Simulations for the Accumulator Design were presented and discussed at *a Space Charge Working group meeting* at CERN, Geneva, on February 27, 2019. Discussions on ESSvSB simulation questions, Ye Zou, Elena Wildner and Maja Olvegård.

3. [The technical planning for the operational phase](#) was presented at the *ESS ILO Network,* 9th March 2019, Lund, Sweden, Mamad Eshraqi.
4. [The Performance of ESSvSB](#) was presented during the *XVIII International Workshop on Neutrino Telescopes (NEUTEL 2019),* 20th March 2019, Venice, Italy, Tord Ekelof.
5. [The ESSvSB Project](#), *The 27th International Workshop on Weak Interactions and* Neutrinos (WIN2019), 3-8 June 2019, Bari, Italy, Budimir Kliček.
6. [The neutrino experiments](#) was presented during the *19th JINR-ISU Baikal Summer School 2019 in Physics of Elementary Particles and Astrophysics*, 11.07. 2019, Baikal, Russia, Marcos Dracos.
7. [Neutrino CP violation with ESSvSB project](#) was presented during *the Division of Particles & Fields of American Physics (DFP 2019*), 1st of August 2019, Boston, USA. Marcos Dracos.
8. [The Neutrino CP Violation with the European Spallation Source neutrino Super Beam](#) project was presented at the *European Society Conference on High Energy Physics (EPS-HEP2019*), 10th of July 2019, Ghent, Belgium, Joakim Cederkall.
9. [The HiRadMat capabilities for ESSvSB future target tests](#) was presented at the *International High Radiations to Materials (HiRadMat 2019),* 10th July 2019, Geneva, Switzerland, Piotr Cupial.
10. [The Neutrino CP Violation with the European Spallation Source neutrino Super Beam](#) was presented at the *19th Lomonosov Conference on Elementary Particle Physics*, the 22nd of August 2019, Moscow, Russia, Marcos Dracos.
11. [The Neutrino CP Violation with the European Spallation Source neutrino Super Beam Project](#) was presented at the *8th International Conference on New Frontiers in Physics (ICNFP 2019),* 22nd August 2019, Kolymbari, Greece, Georgios Fanourakis on behalf of the ESSvSB collaboration.
12. During *the 21st International Workshop on Neutrinos from Accelerators (NUFACT 2019),* Daegu, Korea, 21- 26 August 2019 following talks were presented:
    1. [The ESSvSB project](#), Marcos Dracos
    2. [The Design Study of the Target Station for the ESS Neutrino Super Beam Project](#), Loris D'Alessi.
    3. [The Status of the Detector Design Study for ESSvSB](#) Jason Park.
    4. [The Overview of ESSvSB to Measure δCP](#), Monojit Gosh.
    5. [The Accumulator Ring for the ESSvSB project](#), Ye Zou.
    6. M. Eshraqi and T. Sekiguchi, *WG3 overview*, plenary talk.
    7. [The ESSvSB Linac Design and Beam Dynamics](#), Ben Folsom and B. Gålnander
13. [The Neutrino CP Violation with the European Spallation Source neutrino Super Beam project](#) was presented at the *16th International Conference of Topics in Astroparticle and Underground Physics* (*TAUP 2019),* 9th September 2019, Toyama, Japan, Eirik Gramstad on behalf of the ESSvSB Collaboration.
14. [The neutrino CP violation with the European Spallation source neutrino Super beam"](#) was presented at the *workshop on Connecting Insights in Fundamental Physics*, 31st September 2019, Corfu, Greece. Marcos Dracos.
15. [The Status of the ESSvSB neutrino beam and detector project](#) was presented during the *workshop on Particle with Neutrino Telescopes (PPNT 2019*), 17th October 2019, Uppsala, Sweden, Tord Ekelöf.
16. [The Status of the ESSvSB study](#) was presented at *the J-PARC Symposium*, 26th September 2019, Tsukuba, Japan, Tord Ekelof.
17. ["The ESSvSB Target Station, NBI 2019 Workshop"](#), 22-25 October 2019, Fermilab (USA), E. Baussan.

Posters presented in International Conferences and Workshops

1. [The European Spallation Source neutrino Super Beam](#) was presented during the *Phystatnu International Workshop* 23-25 January 2019, Geneva, Switzerland, Eric Baussan.

2. European Spallation Source Neutrino Super Beam — Physics reach, *XVIII International Workshop on Neutrino Telescopes 2019* (NEUTEL 2019*)*, Venice, Italy, 18-22 March 2019, Toshihiko Ota from the UAM node.
3. European Spallation Source Neutrino Super Beam — Physics reach, *INVISIBLES 19 Workshop*, Valencia, Spain, 10-14 June 2019, Toshihiko Ota from the UAM node.
4. During *the 10th International Particle Accelerator Conference* (IPAC 2019), May 2019, Melbourne, Australia following posters were presented:
   1. Status of the ESSvSB Accumulator Design, Ye Zou.
   2. Status of ESS linac Upgrade studies for ESSvSB, B. Gålnander, M. Eshraqi, C. Martins, R. Miyamoto, A. Farricker and M. Collins
   3. The European Spallation Source neutrino Super Beam Design Study, Marcos Dracos.
   4. Status of the Target Station, Elian Bouquerel.
   5. The ESSvSB Target Station,E. Baussan and al.
5. Neutrino CP Violation with the European Spallation Source neutrino Super Beam project was presented at *the 29th International Symposium on Lepton Photon Interactions at High Energies (LP2019),* Toronto, Canada, 1st August 2019, Marcos Dracos.
6. A poster was presented at the Big Science Business Forum, 28th of March 2019, Copenhagen, Denmark, Tord Ekelof.

Scientific references for the Physics reach section

[1] P. Huber, M. Lindner, and W. Winter, Comput. Phys. Commun. 167, 195 (2005), hepph/0407333.

[2] P. Huber, J. Kopp, M. Lindner, M. Rolinec, and W. Winter, Comput. Phys. Commun. 177, 432 (2007), hep-ph/0701187.

[3] ESSvSB Collaboration, E. Baussan et al., A Very Intense Neutrino Super Beam Experiment for Leptonic CP Violation Discovery based on the European Spallation Source Linac, Nuclear Physics B 885, 127 (2014), 1309.7022.

[4] L. Agostino et al. [MEMPHYS Collaboration],JCAP1301(2013)024 arXiv:1206.6665 [hep-ex].

[5] M. Blennow, P. Coloma and E. Fernandez-Martinez, JHEP 12 (2014) 120 [arXiv:1407.1317].

[6] P. Coloma, P. Huber, J. Kopp and W. Winter, Phys. Rev. D 87 (2013) 3, 033004 [arXiv:1209.5973 [hep-ph]].

[7] I. Esteban, M. C. Gonzalez-Garcia, A. Hernandez-Cabezudo, M. Maltoni and T. Schwetz, JHEP 01 (2019) 106 [arXiv:1811.05487].

[8] J.-E. Campagne, M. Maltoni, M. Mezzetto and T. Schwetz, JHEP 04 (2007) 003 [arXiv:hep-ph/0603172].

[9] M. Honda, T. Kajita, K. Kasahara and S. Midorikawa, Phys. Rev. D70 (2004) 043008 [arXiv:astro-ph/0404457].

[10] S. S. Wilks, Annals Math. Statist. 9 (1938) 60–62.

[11] M. Blennow, P. Coloma and E. Fernandez-Martinez, JHEP 03(2015) 005 [arXiv:1407.3274].

[12] P. Coloma, A. Donini, E. Fernandez-Martinez, and P. Hernandez, JHEP 1206, 073 (2012), arXiv:1203.5651 [hep-ph].

[13] K.N. Abazajian et al. [arXiv:1204.5379].

[14] LSND Collaboration (A. Aguilar-Arevalo et al.), Phys.Rev. D64 (2001) 112007, [arXiv:hep-ex/0104049]